A&A, 692, A129 (2024)
https://doi.org/10.1051/0004-6361/202451049

Astronomy & Astrophysics

The CHEOPS view of the climate of WASP-3 b⋆

G. Scandariato[1,⋆⋆], L. Carone[2], P. E. Cubillos[2,3], P. F. L. Maxted[4], T. Zingales[5,6], M. N. Günther[7], A. Heitzmann[8], M. Lendl[8], T. G. Wilson[9], A. Bonfanti[2], G. Bruno[1], A. Krenn[2], E. Meier Valdes[10], V. Singh[1], M. I. Swayne[11,4], Y. Alibert[10,12], R. Alonso[13,14], T. Bárczy[15], D. Barrado Navascues[16], S. C. C. Barros[17,18], W. Baumjohann[2], W. Benz[12,10], N. Billot[8], L. Borsato[6], A. Brandeker[19], C. Broeg[12,10], M. Buder[20], M.-D. Busch[21], A. Collier Cameron[22], A. C. M. Correia[23], Sz. Csizmadia[24], M. B. Davies[25], M. Deleuil[26], A. Deline[8], L. Delrez[27,28,29], O. D. S. Demangeon[17,18], B.-O. Demory[10,12], A. Derekas[30], B. Edwards[31], D. Ehrenreich[8,32], A. Erikson[24], J. Farinato[6], A. Fortier[12,10], L. Fossati[2], M. Fridlund[33,34], D. Gandolfi[35], K. Gazeas[36], M. Gillon[27], M. Güdel[37], Ch. Helling[2,38], K. G. Isaak[7], L. L. Kiss[39,40], J. Korth[41], K. W. F. Lam[24], J. Laskar[42], A. Lecavelier des Etangs[43], D. Magrin[6], B. Merín[44], C. Mordasini[12,10], V. Nascimbeni[6], G. Olofsson[19], R. Ottensamer[37], I. Pagano[1], E. Pallé[13,14], G. Peter[20], D. Piazza[12], G. Piotto[6,5], D. Pollacco[9], D. Queloz[45,46], R. Ragazzoni[6,5], N. Rando[7], H. Rauer[24,47], I. Ribas[48,49], N. C. Santos[17,18], D. Ségransan[8], A. E. Simon[12,10], A. M. S. Smith[24], S. G. Sousa[17], M. Stalport[28,27], S. Sulis[26], Gy. M. Szabó[30,50], S. Udry[8], V. Van Grootel[28], J. Venturini[8], E. Villaver[13,14], and N. A. Walton[51]

(Affiliations can be found after the references)

Received 10 June 2024 / Accepted 24 September 2024

ABSTRACT

Context. Hot Jupiters are giant planets subject to intense stellar radiation. The physical and chemical properties of their atmosphere make them the most amenable targets for atmospheric characterization.

Aims. In this paper we analyze the photometry collected during the secondary eclipses of the hot Jupiter WASP-3 b by CHEOPS, TESS, and *Spitzer*. Our aim is to characterize the atmosphere of the planet by measuring the secondary eclipse depth in several passbands and constrain the planetary dayside spectrum.

Methods. We updated the radius and the ephemeris of WASP-3 b by analyzing the transit photometry collected by CHEOPS and TESS. We also analyzed the CHEOPS, TESS, and *Spitzer* photometry of the occultations of the planet, measuring the eclipse depth at different wavelengths.

Results. Our update of the stellar and planetary properties is consistent with previous works. The analysis of the occultations returns an eclipse depth of 92±21 ppm in the CHEOPS passband, 83±27 ppm for TESS, and >2000 ppm in the IRAC 1-2-4 *Spitzer* passbands. Using the eclipse depths in the *Spitzer* bands, we propose a set of likely emission spectra that constrain the emission contribution in the CHEOPS and TESS passbands to approximately a few dozen parts per million. This allowed us to measure a geometric albedo of 0.21±0.07 in the CHEOPS passband, while the TESS data lead to a 95% upper limit of ∼0.2.

Conclusions. WASP-3 b belongs to the group of ultra-hot Jupiters that are characterized by a low Bond albedo (<0.3±0.1), as predicted by different atmospheric models. On the other hand, it seems to efficiently recirculate the absorbed stellar energy, which is not typical for similar, highly irradiated planets. To explain this inconsistency, we propose that other energy recirculation mechanisms are at play besides advection (for example, the dissociation and recombination of H_2). Another possibility is that the observations in different bandpasses probe different atmospheric layers; this would make the atmospheric analysis difficult without an appropriate modeling of the thermal emission spectrum of WASP-3 b, which is not feasible with the limited spectroscopic data available to date.

Key words. techniques: photometric – planets and satellites: atmospheres – planets and satellites: detection – planets and satellites: gaseous planets – planets and satellites: individual: WASP-3b

1. Introduction

Hot Jupiters (HJs), giant exoplanets similar to our Solar System's Jupiter in terms of mass and size, are characterized by orbital periods as short as ten days or less. They are thus subject to intense stellar irradiation, which increases their equilibrium temperature by thousands of kelvins compared to their cooler prototype. Moreover, HJs are expected to be tidally locked (Léger et al. 2009) and thus rotate nearly synchronously with their orbits. By consequence, one planetary hemisphere constantly faces the host star, while the other experiences an eternal night. According to theoretical models, this leads to unusual atmospheric dynamics, including vertical stratification, strong winds, and super-rotating equatorial jets (Perryman 2011; Fortney et al. 2021).

Two key parameters that are thought to determine HJ climates are the Bond albedo and the recirculation efficiency (Seager & Dotson 2010; Cowan & Agol 2011; Heng 2017). The Bond albedo quantifies the fraction of incoming stellar radiation that a planet reflects back into space. It sets the energy balance of the planetary atmosphere, impacts the overall climate, and influences circulation patterns in the atmosphere. By studying the

⋆ The CHEOPS program IDs are CH_PR100016 and CH_PR100052.
⋆⋆ Corresponding author; gaetano.scandariato@inaf.it

Table 1. Stellar and system parameters.

Parameter	Symbol	Units	Value	Ref.
V mag			10.63	Høg et al. (2000)
Spectral type			F7V	Street et al. (2007)
Effective temperature	$T_{\rm eff}$	K	6440 ± 120	Montalto et al. (2012)
Surface gravity	$\log g$	$\log c.g.s.$	4.49 ± 0.08	Montalto et al. (2012)
Metallicity	[Fe/H]	–	−0.02 ± 0.08	Montalto et al. (2012)
Projected rotational velocity	$v \sin i$	km/s	13.4 ± 1.5	Montalto et al. (2012)
Stellar radius	$R_\star$	$R_\odot$	1.335 ± 0.010	this work
Stellar mass	$M_\star$	$M_\odot$	1.236 ± 0.040	this work
Stellar age	$t_\star$	Gyr	$1.5^{+0.9}_{-0.8}$	this work

albedo, we gain insights into the planet's atmospheric properties, such as cloud cover, atmospheric composition, and scattering behavior. A high albedo suggests reflective surfaces (e.g., silicate clouds; Sudarsky et al. 2000), while a low albedo implies absorption.

The recirculation efficiency refers instead to how efficiently a planet redistributes the absorbed energy from its dayside to its nightside. A high recirculation efficiency implies an effective heat redistribution, which leads to more uniform temperatures across the planet. Conversely, a low efficiency results in stark day–night temperature contrasts. By constraining the recirculation efficiency, we can understand atmospheric circulation patterns, including jet streams, winds, and other heat transport mechanisms (see, e.g., Cowan & Agol 2011).

WASP-3 b is a prototypical HJ and was first reported by Pollacco et al. (2008). Its close orbit, its large radius, and the high effective temperature of its host star place WASP-3 b in the group of strongly irradiated HJs. It is thus an extremely interesting target for albedo and recirculation measurements that would enhance our understanding of the planetary climate and inform theoretical atmospheric models.

For this reason, WASP-3 b was observed as part of the guaranteed time observation (GTO) program of the CHEOPS (CHaracterising ExOPlanet Satellite) mission (Benz et al. 2021; Fortier et al. 2024). This program was aimed at detecting secondary eclipse HJs, which can be used to directly constrain the reflectivity of a planetary atmosphere. Since the beginning of the mission, this program has proved CHEOPS's capacity to retrieve faint eclipse signals on the order of tens to hundreds of parts per million (see for example Lendl et al. 2020; Brandeker et al. 2022). In some cases, when data from other facilities operating at different wavelengths were available, CHEOPS optical observations helped in constraining the climate properties of several HJs (see for example Scandariato et al. 2022; Parviainen et al. 2022; Singh et al. 2022; Hoyer et al. 2023; Pagano et al. 2024).

We present the atmospheric characterization of WASP-3 b using CHEOPS observations and other public space photometry data: TESS (Transiting Exoplanet Survey Satellite) in the optical and *Spitzer* in the infrared. Firstly, we revise the stellar parameters in Sect. 2. We present the CHEOPS, TESS, and *Spitzer* photometric datasets in Sect. 3 and their analysis in Sect. 4; there, we update the orbital parameters and measure the planetary radius and the secondary eclipse depths. In Sect. 5 we combine the derived system parameters to constrain the albedo and recirculation efficiency of WASP-3 b and discuss the implications for its climate. We conclude with our final remarks in Sect. 6.

2. Stellar radius, mass, and age

The atmospheric stellar parameters were taken from Montalto et al. (2012) since there were no additional higher quality spectra available in public spectra archives.

To determine the stellar radius of WASP-3, we used broadband photometry from *Gaia* G, $G_{\rm BP}$, and $G_{\rm RP}$, 2MASS J, H, and K, and WISE $W1$ and $W2$ (Skrutskie et al. 2006; Wright et al. 2010; Gaia Collaboration 2023) and the stellar spectral parameters listed in Table 1 in a modified Markov chain Monte Carlo infrared flux method framework (Blackwell & Shallis 1977; Schanche et al. 2020). We produced synthetic photometry from constructed spectral energy distributions built using stellar atmospheric models from the ATLAS catalog (Castelli & Kurucz 2003) and fitted them to the observations to derive the stellar bolometric flux. We converted this to the stellar effective temperature and angular diameter, and finally the stellar radius using the offset-corrected *Gaia* parallax (Lindegren et al. 2021).

The effective temperature, the metallicity, and the radius along with their uncertainties constitute the basic input set to derive the isochronal mass ($M_\star$) and age ($t_\star$) of the star. To this end, we employed the isochrone placement algorithm (Bonfanti et al. 2015, 2016) to interpolate the input parameters within two different sets of grids of isochrones and tracks generated using two different stellar evolutionary codes, namely PARSEC[1] v1.2S (Marigo et al. 2017) and CLES (Scuflaire et al. 2008). For each set of grids we computed a mass and an age estimate, and after merging the two respective pairs of outcome following the statistical treatment outlined in Bonfanti et al. (2021), we obtained $M_\star = 1.236 \pm 0.040\, M_\oplus$ and $t_\star = 1.5^{+0.9}_{-0.8}$ Gyr.

3. Observations and data reduction

3.1. TESS observations

Observations of WASP-3 by the TESS mission (Ricker et al. 2015) with a cadence of 120 s are available for 5 sectors (26, 40, 53, 54, 74) covering 54 transits and 57 secondary eclipses. These observations span the date range 2020-06-09 to 2024-01-30.

We used the pre-search data conditioning SAP fluxes (PDC-SAP_FLUX) available from the TESS Science Processing Operations Centre (SPOC) and downloaded using the software package LIGHTKURVE 2.0 (Lightkurve Collaboration 2018)[2]. Our

[1] *PA*dova & *TR*ieste *S*tellar *E*volutionary *C*ode: http://stev.oapd.inaf.it/cgi-bin/cmd

[2] https://lightkurve.github.io/lightkurve/

Table 2. Log of CHEOPS observations.

	File key	Event [a]	Start date (UTC)	Dur. [b] (h)	Eff. [c] (%)	Decorrelation parameters [d]
1	CH_PR100016_TG014001_V0200	Ecl.	2021-07-03T07:32:18	10.45	66	x, y, $\sin\phi$, $\sin 2\phi$, $\sin 3\phi$, $\cos 3\phi$
2	CH_PR100016_TG014002_V0200	Ecl.	2021-07-05T02:27:59	10.50	65	y, $\cos\phi$
3	CH_PR100016_TG014003_V0200	Ecl.	2021-07-06T23:13:58	11.91	65	bg, t, $\cos\phi$, $\cos 2\phi$
4	CH_PR100016_TG014004_V0200	Ecl.	2021-07-08T19:34:58	10.42	65	x, y, $\sin\phi$, $\sin 2\phi$, $\sin 3\phi$
5	CH_PR100016_TG014005_V0200	Ecl.	2021-07-10T17:11:38	10.24	65	$\sin\phi$, $\sin 2\phi$, $\sin 3\phi$
6	CH_PR100016_TG014006_V0200	Ecl.	2021-07-12T12:09:58	10.45	65	bg, $\cos 2\phi$, $\cos 3\phi$
7	CH_PR100016_TG014007_V0200	Ecl.	2021-07-19T22:35:58	10.49	67	y, t, $\sin\phi$, $\sin 3\phi$
8	CH_PR120052_TG002201_V0200	Tr.	2022-06-22T02:27:39	3.17	67	$\sin\phi$, $\cos\phi$
9	CH_PR100016_TG014008_V0200	Ecl.	2022-06-22T21:43:39	10.49	66	bg, x, $\sin\phi$, $\cos 2\phi$, $\sin 3\phi$
10	CH_PR120052_TG002202_V0200	Tr.	2022-06-23T23:37:38	2.57	79	$\cos\phi$,$\sin 2\phi$, $\cos 2\phi$
11	CH_PR120052_TG002203_V0200	Tr.	2022-06-25T18:41:00	3.17	59	y, $\cos 2\phi$
12	CH_PR100016_TG014009_V0200	Ecl.	2022-06-26T14:37:39	10.62	66	y, $\sin\phi$, $\cos 3\phi$
13	CH_PR100016_TG014010_V0200	Ecl.	2022-07-09T12:18:59	10.59	65	t, $\sin\phi$, $\sin 3\phi$
14	CH_PR100016_TG014011_V0200	Ecl.	2022-07-13T04:06:59	12.06	67	x, y, t, $\sin\phi$
15	CH_PR120052_TG002204_V0200	Tr.	2022-07-14T05:59:58	2.68	78	y, $\cos\phi$, $\sin 3\phi$
16	CH_PR100016_TG014012_V0200	Ecl.	2022-07-15T00:13:59	10.82	70	x, bg, $\sin\phi$

Notes. [a]Either a secondary eclipse (Ecl.) or a transit (Tr.). [b]The duration of the observing interval. [c]The fraction of the observing interval covered by valid observations of the target. [d]This column reports the variables used for the de-correlation against the instrumental noise: spacecraft roll angle, ϕ, time, t, image background level, bg, and the centroid of the target PSF on the detector (x,y).

analysis improves on the results of Wong et al. (2021), who analyzed only sector 26, the only one available at the time of their writing.

3.2. CHEOPS observations

We observed 12 complete secondary eclipses of WASP-3 b as part of the GTO program ID-016 "Occultations". WASP-3 was also included in the GTO program ID-052 "Short-period EBLM and hot-Jupiter systems". This is a "filler" program that makes use of gaps between other GTO programs. The four observations of a few hours each from the filler program do not cover complete transits by themselves, but do cover the full orbital phase range of the transit when taken together. Observations from both programs used an exposure time of 60 s. The log of the observations is shown in Table 2.

The data used here were processed using version 13 of the CHEOPS data reduction pipeline (DRP; Hoyer et al. 2020). We used light curves (LCs) generated from the CHEOPS imagettes with the point spread function (PSF) photometry package PIPE[3] developed specifically for CHEOPS (Brandeker et al., in prep.; Szabó et al. 2021; Morris et al. 2021). Previous studies have shown that PIPE LCs give results that are consistent with LCs computed using synthetic aperture photometry by the DRP but typically with improved precision because the PIPE LCs are less affected by instrumental noise (Brandeker et al. 2022; Oddo et al. 2023; Krenn et al. 2023).

3.3. Spitzer observations

The *Spitzer* Space Telescope observed four eclipses LCs of WASP-3 b from three visits (Table 3). All observations were carried out using the Infrared Array Camera (IRAC) instrument (Fazio et al. 2004), sampling three different bands. The 2008 observations were obtained during the cryogenic mission, in full-array mode, with a cadence of 12.0 s per frame. The 2009 and 2016 observations were obtained during the warm mission, in sub-array mode, with a cadence of 2.0 s per frame.

Table 3. *Spitzer* secondary eclipse observations of WASP-3 b.

Band (λ)	Date	PI (program)
IRAC 2 (4.5 μm)	2008-09-18	P. Wheatley (50759)
IRAC 4 (8.0 μm)	2008-09-18	P. Wheatley (50759)
IRAC 1 (3.6 μm)	2009-10-26	H. Knutson (60021)
IRAC 2 (4.5 μm)	2016-11-10	D. Deming (13044)

4. Data analysis

4.1. TESS light curve analysis

We performed the analysis of the TESS LCs using PlanetModel model in `pycheops` (Maxted et al. 2022)[4]. This model uses the qpower2 algorithm (Maxted & Gill 2019) to compute the LCs for the transit assuming the power-2 limb-darkening law, $I_\lambda(\mu) = 1 - c\,(1-\mu^\alpha)$, where μ is the cosine of the angle between the surface normal and the line of sight. The flux from the planet is calculated using a Lambertian phase function, and the secondary eclipse due to the occultation of this reflected flux is computed assuming a uniform disk for the planet. There is no evidence for any orbital eccentricity in the orbit of WASP-3 b from either the radial velocity measurements or the phase of the secondary eclipse, so we also assumed that the planet has a circular orbit, as is typical for short-period HJ systems (Bonomo et al. 2017). We only used data from within one transit duration of the times of mid-transit or mid-eclipse, which resulted in 18 812 observations being used for this analysis. The flux values for each transit or secondary eclipse were divided by a robust

[3] https://github.com/alphapsa/PIPE

[4] https://github.com/pmaxted/pycheops

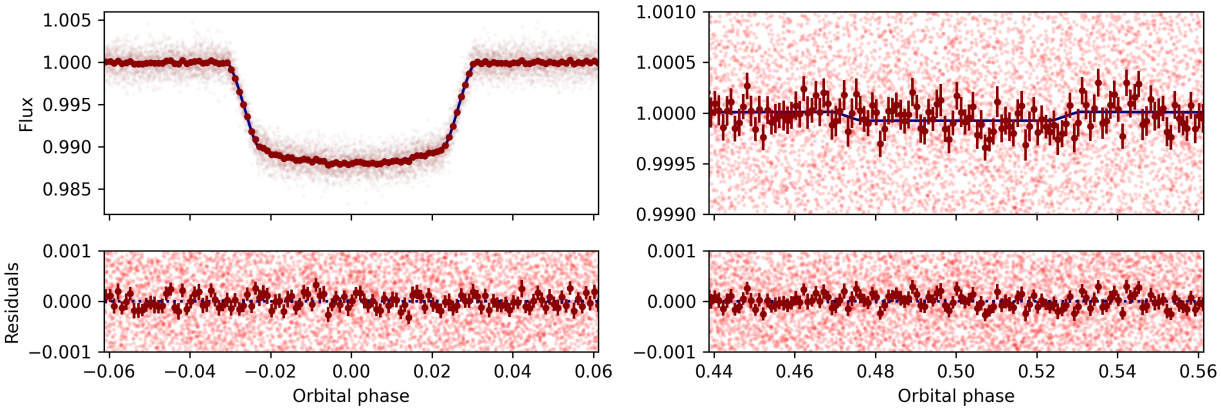

Fig. 1. Phase-folded TESS LC of WASP-3 (pale red points) centered on the planetary transit (left column) and secondary eclipses (right column). Our best-fit model is shown with a dark blue line. The dark red points show the mean value of the observations and residuals in bins of 0.001 phase units (160 s).

straight-line fit (Siegel 1982) to the flux values on either side of the primary or secondary eclipse. There is no evidence of variability in the TESS LC between the transits on the timescales expected for stellar rotation. The amplitude of any such variability is less than 500 ppm; therefore, WASP-3 is not a magnetically active star and so we do not expect any significant variability in the transits due to the planet occulting star spots.

We used the CHEOPS exposure time calculator[5] to estimate that the granulation noise on a timescale of 3 hours is 15 ppm. This is an order of magnitude smaller than the white noise and a factor of a few less than the eclipse depth, so we assumed a Gaussian white-noise model with equal standard deviations σ_w for each observation. The free parameters in the fit are: the time of mid-transit, T_0; the orbital period, P; the transit impact parameter, $b = a\cos(i)/R_\star$ where a is the orbital semimajor axis and i is the orbital inclination; the transit depth parameter, $D = (R_{\rm pl}/R_\star)^2 = k^2$; the transit width, $W = (R_\star/a)\sqrt{(1+k)^2 - b^2}/\pi$; the limb-darkening parameter $h_1 = I_\lambda(\frac{1}{2}) = 1 - c(1 - 2^{-\alpha})$; the planet's geometric albedo assuming zero thermal emission, $A_{g,0}$; the log of the standard error per observation, $\log\sigma_w$. We assume uniform priors on $\cos i$, $\log k$, $\log a/R_\star$. The limb-darkening parameter $h_2 = I_\lambda(\frac{1}{2}) - I_\lambda(0) = c2^{-\alpha}$ has a negligible effect on the quality of the fit and so was fixed at the value $h_2 = 0.44$, appropriate for a star of this type (Maxted 2018). All other parameters have broad uniform priors. To sample the posterior probability distribution (PPD) of the model parameters we used `emcee` (Foreman-Mackey et al. 2013) with 64 walkers and 256 steps after 512 burn-in steps. Convergence of the sampler was checked by visual inspection of the sample values for each parameter and each walker as a function of step number. The mean and standard error for each parameter calculated from the samples' PPD are given in Table 4 and the best fit to the LCs is shown in Fig. 1. Correlations between selected parameters from the PPD are shown in Fig. 2. The parameter of interest is the eclipse depth,

$$\delta_{\rm ecl} = A_{g,0}\left(\frac{R_{\rm pl}}{a}\right)^2, \quad (1)$$

so we also quote this value in Table 4. We also tried a model with zero albedo and pure thermal emission from the planet and found that there was a negligible change in the results (i.e., the value of $\delta_{\rm ecl}$ derived is insensitive to the details of the model used to describe the flux from the planet).

[5] https://cheops.unige.ch/pht2/exposure-time-calculator/

Table 4. Results from our fit to TESS LCs of WASP-3.

Parameter [(a)] (Unit)	Value
T_0 ($\rm BJD_{TDB}$)	2459606.789477 ± 0.000052
P (days)	1.8468354 ± 0.0000002
D	0.011043 ± 0.000054
W (phase)	0.06118 ± 0.00012
b	0.510 ± 0.015
$A_{g,0}$	0.195 ± 0.063
h_1	0.828 ± 0.007
h_2 [(b)]	= 0.44
$\ln\sigma_w$	−6.736 ± 0.005
Derived parameters	
$k = R_{\rm pl}/R_\star$	0.10509 ± 0.00026
$a/R_\star$	5.099 ± 0.047
$\delta_{\rm ecl}$ (ppm)	83 ± 27
$\sigma_{\rm w}$ (ppm)	1188 ± 6
$T_{\rm irr} = T_{\rm eff}\sqrt{R_\star/a}$ (K)	2850 ± 50

Notes. [(a)]T_0 is the time of mid-transit, P is the orbital period, $D = (R_{\rm pl}/R_\star)^2$ is the transit depth, W is the transit width, b is the transit impact parameter, $A_{g,0}$ is the planet's geometric albedo assuming zero thermal emission, h_1 and h_2 are the parameters of the power-2 limb-darkening law, σ_w is the standard error per observation, a is the orbital semimajor axis, and $\delta_{\rm ecl}$ is the eclipse depth. [(b)]Fixed parameter.

4.2. CHEOPS light curve analysis

We analyzed the CHEOPS LCs of WASP-3 produced using PIPE PSF photometry using `pycheops` version 1.1.8. The model and assumptions are the same as for the analysis of the TESS photometry (Sect. 4.1).

This version of `pycheops` is fundamentally the same as the version described in Maxted et al. (2022), but includes a number of functions that were introduced in `pycheops` version 1.1.0 that make it easier to analyze CHEOPS LCs. For example, `pycheops` can now create dataset objects that contain LCs and metadata for a single visit directly from PIPE output files, and includes a new method, MultiVisit.fit_planet(), that can be used to analyze

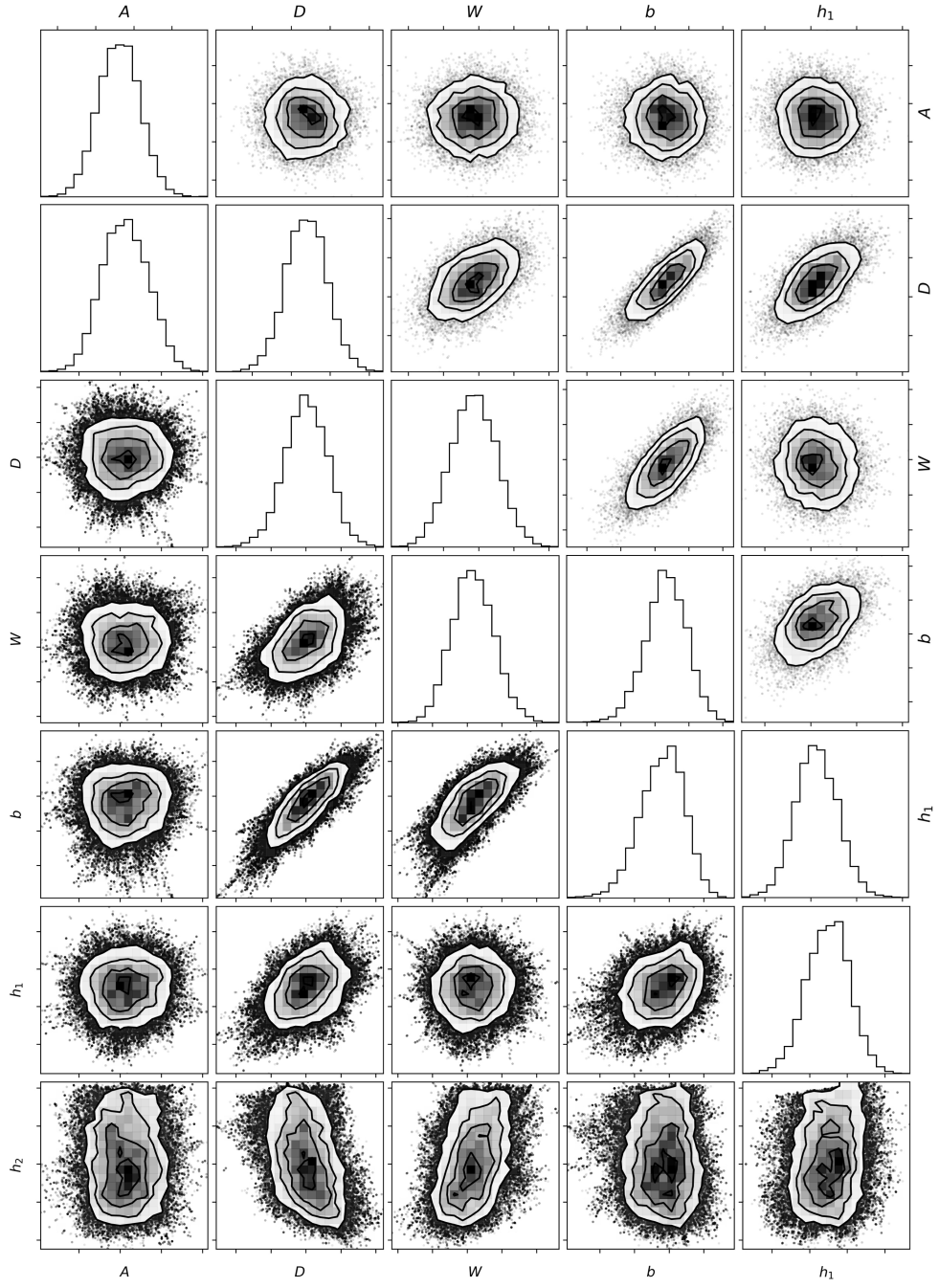

Fig. 2. Parameter correlation plots for selected parameters from our analysis of the CHEOPS (lower left) and TESS (upper right) LCs of WASP-3.

multiple dataset objects covering transits and secondary eclipses using the PlanetModel model described above.

We use a linear model of the form $c(1 + \sum_k a_k d_k(t))$ to describe the instrumental noise in the LC for each dataset object. The complete model for the LC is a PlanetModel LC multiplied by this linear instrumental noise model. The basis vectors $d_k(t)$ are generated from the house-keeping data provided in the dataset (e.g., $\sin\phi, \cos\phi, \sin 2\phi$, etc., where ϕ is the spacecraft roll angle). To select basis vectors that give a significant improvement to the quality of the fit, we computed the Bayes factor,

$$B_k = e^{-(a_k/\sigma_k)^2/2}\,\sigma_0/\sigma_k.$$

The parameters a_k ("detrending coefficients") are assumed to have Gaussian priors with mean 0 and standard deviation σ_k. For a model where a_k is included as a free parameter, a_k in this equation is the best-fit (maximum likelihood) value and σ_k is its standard error. If we set σ_0 to the standard deviation of the residuals from a model with no instrumental noise model, we find that free parameters with $B_k > 0.5$ give a negligible improvement to the quality of the fit, are poorly constrained, have a best-fit value consistent with 0, and have a negligible impact on the results obtained. We therefore only include detrending coefficients as free parameters in the instrumental noise model if their Bayes factor is $B_k < 0.5$. Detrending coefficients should be selected one-by-one, recomputing the Bayes factor for each new model. This can be done automatically in `pycheops` version 1.1.0 using the new feature Dataset.select_detrend(). The basis vectors selected for the instrumental noise model for each visit are listed in Table 2. We excluded the coefficient for the basis vector $f(t) = t^2$ because this tends to be degenerate with

the model for the secondary eclipse, and including this term is not justified for the short visits that cover the transits.

To model the residual noise in the LCs, we assume a white-noise model where the variance on the flux measurement f_i is $\sigma_i^2 + \sigma_w^2$, where σ_i is the standard error estimate provided with the data that quantifies known noise sources (photon-counting noise, read-out noise, etc.), and the extra white-noise contribution σ_w is assumed to be the same for all observations and for all visits. These errors are assumed to be normally distributed and independent. CHEOPS is able to detect variability due to granulation or solar-like pulsations in solar-type stars brighter than $V \approx 6.5$ (Sulis et al. 2023). WASP-3 is much fainter than this limit (V = 10.6) so correlated noise due to granulation or solar-like pulsations will be undetectable in the CHEOPS data. There is also very little correlated noise due to the instrument or data reduction apart from the trends captured by the instrument noise model described above (Fortier et al. 2024).

All the datasets listed in Table 2 were analyzed together using MultiVisit.fit_planet(). The observed flux values for each dataset were first corrected for instrumental noise using the best-fit instrumental noise model prior to this joint analysis ("unwrap = True" option in MultiVisit.fit_planet()). The orbital period was fixed at the value $P = 1.84683542$ days taken from the analysis of the TESS LC. MultiVisit.fit_planet() includes the option to implicitly include trends correlated with space-craft roll angle using a harmonic series with $n_{\rm roll}$ terms. We tried models including values of $n_{\rm roll}$ up to 4, but found that none of these models significantly improved the quality of the fit and the change in the results for the parameters of interest is negligible, so we did not use this option for the results presented here.

Previous studies using CHEOPS LCs have used a variant of the SCALPELS algorithm (Collier Cameron et al. 2021) to generate basis vectors from the PSF autocorrelation function that can be used to generate a linear model for instrumental noise associated with changes in the shape of the PSF (Wilson et al. 2022). We calculated SCALPELS basis vectors for all our observations of WASP-3 with CHEOPS and tested whether they provide a significant improvement to the quality of the fit if we include them in the instrumental noise model. This was straightforward to do using the new extra_decorr_vectors functionality that was added to the fitting routines in `pycheops` for version 1.1.0. We find that the quality of the fit is not significantly improved for any of the visits if we include these extra basis functions, and the results we obtain are indistinguishable from the results presented here if we do include the few SCALPELS basis functions that provide a marginal improvement to the quality of the fit. We therefore decided, for simplicity, to present results here that do not include SCALPELS basis vectors in the instrumental noise model for any of the visits.

We assumed uniform priors on $\cos i$, $\log k$, $\log a/R_\star$ across the full allowed range of these parameters. All other parameters have broad uniform priors around their best-fit values from a previous fit to the CHEOPS data. We included h_2 as a free parameter to the CHEOPS LC because the parameter is constrained by the data and the value obtained is reasonable for a star of this type. To sample the PPD of the model parameters we used `emcee` with 256 walkers and 1024 steps after 2048 burn-in steps. Convergence of the sampler was checked by visual inspection of the sample values for each parameter and each walker as a function of step number. The mean and standard error for each parameter calculated from the samples PPD are given in Table 5 and the best fit to the LC is shown in Fig. 3. Correlations between selected parameters from the PPD are shown in Fig. 2.

Table 5. Results from our fit to the CHEOPS LC of WASP-3.

Parameter (Unit)	Value
D	0.01095 ± 0.00016
W (phase)	0.06134 ± 0.00033
b	0.487 ± 0.033
$A_{g,0}$	0.222 ± 0.053
T_0 ($\mathrm{BJD_{TDB}}$)	$2459606.78941 \pm 0.00010$
h_1	0.748 ± 0.012
h_2	0.53 ± 0.15
$\ln \sigma_w$	-8.010 ± 0.024
df/dx_1	0.00049 ± 0.00014
df/dy_1	-0.00081 ± 0.00012
df/dt_1	0.00056 ± 0.00021
df/dy_2	-0.00035 ± 0.00011
$df/d\mathtt{bg}_3$	-0.00064 ± 0.00026
df/dt_3	0.00067 ± 0.00018
df/dx_4	0.00041 ± 0.00014
df/dy_4	-0.00089 ± 0.00012
$df/d\mathtt{bg}_6$	-0.00081 ± 0.00021
df/dy_7	-0.00052 ± 0.00010
df/dt_7	0.00094 ± 0.00020
$df/d\mathtt{bg}_9$	0.00120 ± 0.00018
df/dx_9	0.00052 ± 0.00015
df/dy_{11}	-0.00103 ± 0.00024
df/dy_{12}	0.00077 ± 0.00013
df/dt_{13}	-0.00091 ± 0.00020
df/dx_{14}	0.00099 ± 0.00014
df/dy_{14}	-0.00131 ± 0.00011
df/dt_{14}	-0.00042 ± 0.00017
df/dy_{15}	-0.00126 ± 0.00023
$df/d\mathtt{bg}_{16}$	0.00052 ± 0.00020
df/dx_{16}	0.00067 ± 0.00017
Derived parameters	
$\delta_{\rm ecl}$ (ppm)	92 ± 21
$k = R_{\rm pl}/R_\star$	0.10464 ± 0.00075
$\sigma_{\rm w}$ (ppm)	332 ± 8

Notes. Detrending coefficients are labeled using the notation df/dq_i for quantity q in dataset i, as listed in Table 2.

4.3. Masses and radii

We computed the mass and radius of WASP-3 b using the average values of the parameters k, $\sin i$ and $a/R_\star$ from Tables 4 and 5 and their standard errors computed using the "combine" algorithm described in Appendix A of Maxted et al. (2022). The semi-amplitude of the star's spectroscopic orbit used to compute the planet's mass, $K_{\rm rv}$, is the weighted mean of the values derived by Pollacco et al. (2008) and Maciejewski et al. (2013). It should be noted that we did not use the value of $R_\star$ from Table 1 in this calculation because this quantity follows directly from the mean stellar density that can be computed from P and $a/R_\star$. The results are given in Table 6. The agreement between the radius derived from the mean stellar density ($1.332 \pm 0.018\,R_\odot$) and the independent estimate given in Table 1 ($1.335 \pm 0.010\,R_\odot$) is better than 1σ.

4.4. Spitzer light curve analysis

We analyzed the *Spitzer* data using the Photometry for Orbits, Eclipses, and Transits (POET) pipeline (Stevenson et al. 2010,

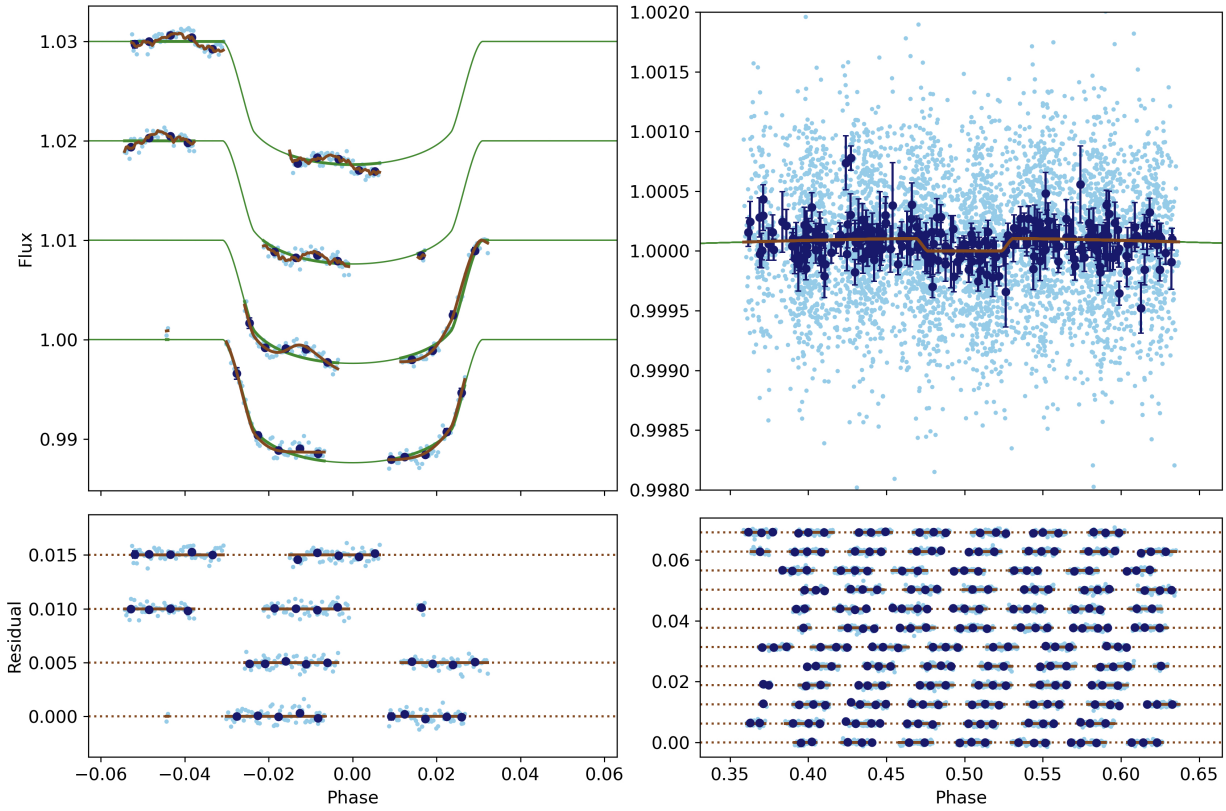

Fig. 3. CHEOPS LC of WASP-3 and our best-fit model for the transits and eclipses. Upper-left panel: observed transit LCs (in cyan) offset vertically by multiples of 0.01 units. The dark blue points are the data points binned over 0.01 phase units. The full model, which includes instrumental trends, is shown in brown, and the transit model without trends is shown in green. Lower-left panel: residuals from the best-fit model to the transit LCs offset vertically by multiples of 0.005 units. Upper-right panel: Secondary eclipse LCs after removal of instrumental noise from our best-fit model, plotted without any vertical offset. Lower-right panel: residuals from the best-fit model to the secondary eclipses offset vertically by multiples of 0.005 units.

Table 6. Mass and radius estimates for WASP-3 and WASP-3 b as inferred from the transit observables.

Parameter	Units	Value	Error
Input values			
P	(d)	1.8468354	
$M_\star$	($M_\odot$)	1.236	± 0.040
K_{RV}	($m\,s^{-1}$)	259	± 7
e		0 (fixed)	
$\sin i$		0.9951	± 0.0004
$R_{pl}/R_\star$		0.10503	± 0.00027
$a/R_\star$		5.108	± 0.043
Derived quantities			
$R_\star$	($R_\odot$)	1.332	± 0.018
M_{pl}	(M_{Jup})	1.811	± 0.063
R_{pl}	(R_{Jup})	1.392	± 0.019
g_{pl}	($m\,s^{-2}$)	24.2	± 0.8
ρ_{pl}	($g\,cm^{-3}$)	0.891	± 0.035
$T_4 - T_1$	(d)	0.114	± 0.002
$T_3 - T_2$	(d)	0.085	± 0.002
$T_{irr} = T_{eff}\sqrt{\frac{R_\star}{a}}$	(K)	2850	± 50

Notes. $R_{Jup} = 69911$ km is the volume-average radius of Jupiter. $T_4 - T_1$ and $T_3 - T_2$ are the time intervals between the contact points of the primary eclipse (transit).

2012a,b; Campo et al. 2011; Nymeyer et al. 2011; Cubillos et al. 2013, 2014). The POET pipeline consists of two main stages, first it extracts raw LCs from the 2D time-series images, and then it models the LCs to constrain the eclipse properties.

Stage one of the POET analysis starts by reading the *Spitzer* basic calibrated data (BCD), produced by the *Spitzer* pipeline version 18.25.0 for the 2008 observation and version 19.2.0 for the 2009 and 2016 observations. The BCD data provide the science images, uncertainty images, and bad-pixel masks. Next, POET flags bad pixels from the *Spitzer* BCD files using the bad-pixel masks and performing a sigma-rejection routine for outlier pixel values. As the 2008 observation consists of instrument engineering request data, mask files are not associated with each science image. Therefore, we performed a more careful sigma-rejection step to flag pixels showing transient fluctuations away from the median of the neighboring ten frames. Then, POET estimates the target center position on the detector by fitting a 2D Gaussian function. Finally, POET obtains raw LCs by applying interpolated aperture photometry and testing several circular apertures with radii ranging from 1.5 to 4.5 pixels in 0.25 pixel increments.

In stage two, POET models the raw LCs by simultaneously fitting the astrophysical signal (i.e., the eclipse) and the instrumental systematics. To model the astrophysical signal we used a Mandel & Agol (2002) eclipse model. The free fitting parameters of this model are the stellar flux, the eclipse mid-point epoch, duration, depth, and ingress duration (setting the egress duration equal to the ingress duration). We adopt uniform prior

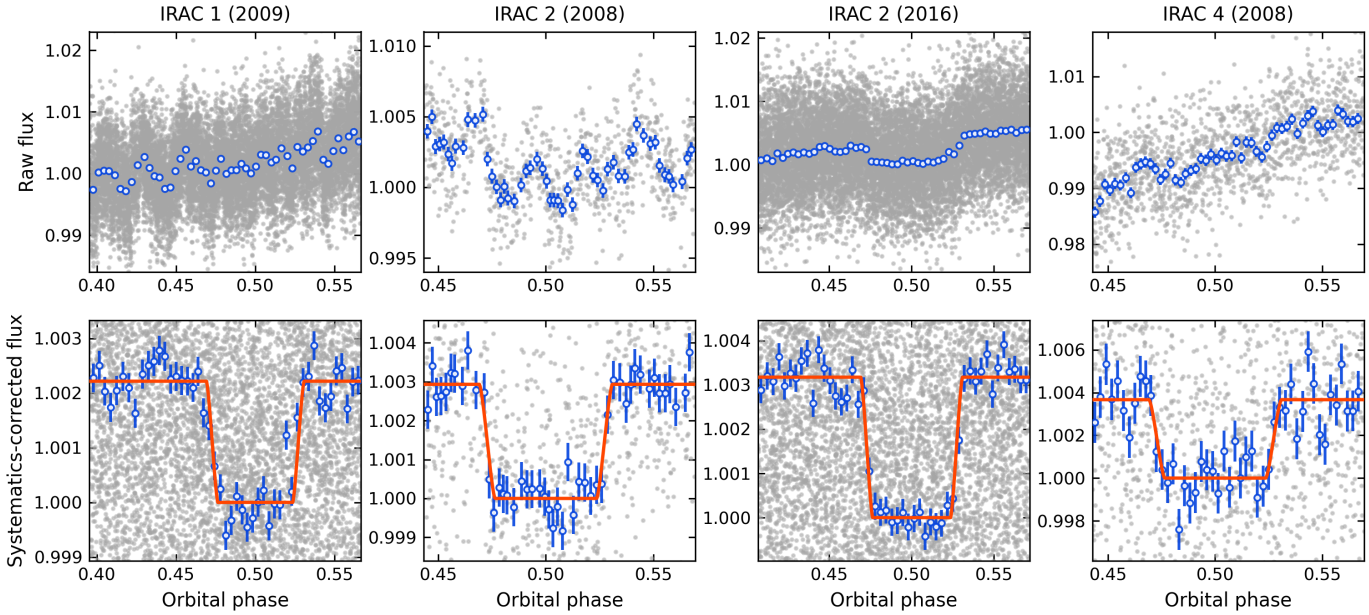

Fig. 4. Normalized *Spitzer* LCs of WASP-3 after the raw aperture-photometry extraction (top panels) and after removing instrumental systematics from the joint LC fit (bottom panels). The gray markers show the flux of the individual frames, whereas the blue markers show the binned fluxes and their uncertainties. The red curves in the bottom panels show the best-fit eclipse model for each observation.

for all parameters. The IRAC detectors typically exhibit temporal and intra-pixel sensitivity variations (Charbonneau et al. 2005). To model the temporal instrumental systematics we tested several parametric "ramp" models as a function of time (linear, quadratic, and exponential ramps). To model the intra-pixel systematics we employed the bi-linearly interpolated sub-pixel sensitivity (BLISS) map model (Stevenson et al. 2012a).

The final LC model is then composed of the multiplicative factors of the astrophysical, ramp, and intra-pixel models. Using the MC3 statistical package (Cubillos et al. 2017), POET determines parameter's best-fitting values (via a trust region reflective optimization) and their Bayesian posterior distributions (via the differential-evolution Markov chain Monte Carlo sampler ter Braak & Vrugt 2008). The Markov chain uses the Gelman-Rubin statistic (Gelman & Rubin 1992) to be within 1% of unity to assess parameter convergence.

We analyzed the LCs in two steps. First we modeled each independent observation to determine the optimal aperture photometry radii and optimal systematic models. Then we performed a joint-fit analysis of all four observations to determine the final values. We selected the optimal systematics model by minimizing the Bayesian information criterion (Schwarz 1978) from a set of fits to a given dataset. Here we tested fits with and without a BLISS model, and we tested fits with each of the different ramp models: linear, quadratic, exponential, or no ramp. We selected the optimal aperture photometry by minimizing the standard deviation of the residual between the raw LC and their respective best-fitting model. We also paid attention to the time-correlated noise by computing the Allan deviation (also known as time-averaging method, Allan 1966), finding no significant deviation for any of the datasets. Table 7 lists the preferred aperture radii and systematics models for each individual observation.

To obtain final eclipse depths we ran a joint fit combining all four events. In this fit, we shared the mid-eclipse epoch, duration, and ingress-time parameters among all events. The combined analysis thus enables a more robust estimation of the eclipse LC shape of the individual observations. Figure 4 shows the systematics-corrected LC data and joint best-fitting model. Table 7 presents the retrieved values for the astrophysical parameters, derived from the posterior distribution (median and central 68% percentile).

The *Spitzer* transit depths analyzed with POET are consistent with those of Rostron et al. (2014) within 1σ, though we consistently obtain deeper occultation depths. From the occultation depths we can estimate a planetary brightness temperature at each band. As expected, we find a similar trend as Rostron et al. (2014), that is, a deeper occultation depth at 4.5 μm than at 3.6 or 8.0 μm (Table 7). To the first order, the *Spitzer* observations do not deviate much from a blackbody spectrum for the planet. In the following section we perform a more in-depth physical interpretation of the observations.

We also compared our results to the population-level analysis of *Spitzer* secondary analyses by Deming et al. (2023), who used more modern pixel-level de-correlation (PLD) method to detrend the telescope systematics (Deming et al. 2015). They reported depths of $0.229 \pm 0.011\%$ at 3.6 μm, $0.273 \pm 0.016\%$ at 4.5 μm (2008), and $0.290 \pm 0.012\%$ at 4.5 μm (2016) (see our Fig. 5 for a graphical comparison). While our 3.6 μm occultation depths are consistent within the uncertainty, at 4.5 μm we obtained depths that are ∼1.5 and 2σ deeper (2008 and 2016 epochs, respectively). This is intriguing, given that both the BLISS and PLD methods are among the most robust and accurate noise-retrieval techniques for *Spitzer* time-series observations (Ingalls et al. 2016). We thus conjecture that the discrepancies arise from other assumptions made during the LC analysis. Since Deming et al. (2023) analyzed the entire population of *Spitzer* occultations for HJs, they did not provide the specific details of the WASP-3 b analyses. Therefore, we are forced to draw our conclusions based on their general analysis description (Appendix A). We identified two significant differences between our analysis approaches. One is that Deming et al. (2023) adopted a quadratic ramp for all planets with equilibrium temperature greater than 2000 K (this includes WASP-3 b). From our individual-epoch

Table 7. *Spitzer* LC observations of WASP-3.

Parameter	IRAC 1 (2009)	IRAC 2 (2008)	IRAC 2 (2016)	IRAC 4 (2008)
Aperture radius (pixels)	2.00	2.25	2.25	2.75
BLISS model	Yes	Yes	Yes	No
Ramp model	Quadratic	Linear	None	Exponential
$\delta_{\rm ecl}$ (%)	$0.224^{+0.014}_{-0.013}$	$0.295^{+0.015}_{-0.015}$	$0.320^{+0.014}_{-0.015}$	$0.369^{+0.049}_{-0.051}$
$T_{\rm bright}$ (K)	2361 ± 66	2460 ± 72	2575 ± 67	2390 ± 220
Mid-eclipse epoch$^{(\dagger)}$	$0.49995^{+0.00028}_{-0.00031}$	–	–	–
Eclipse duration$^{(\dagger)}$ ($T_4 - T_1$)	$0.0627^{+0.0022}_{-0.0016}$	–	–	–
Ingress time$^{(\dagger)}$ ($T_2 - T_1$)	$0.0082^{+0.0021}_{-0.0015}$	–	–	–

Notes. $^{(\dagger)}$ Free parameter shared between all four *Spitzer* observations. The units are in orbital phase relative to the transit epoch and period from Table 6.

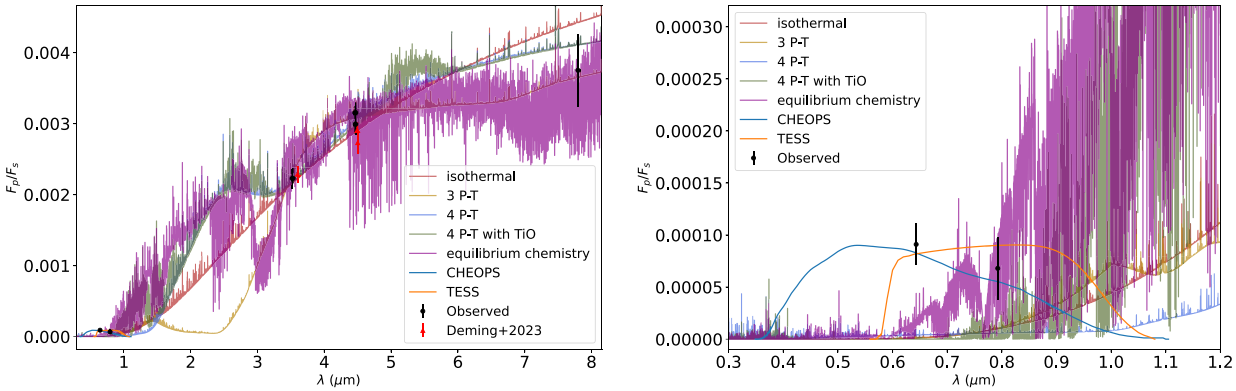

Fig. 5. Emission spectra with different model assumptions. Left: all the best-fit models we performed in this work. The black points represent the observations with TESS, CHEOPS, and *Spitzer*, while red points show the measurements by Deming et al. (2023). Right: zoomed-in view of the optical wavelength, together with the TESS and CHEOPS observations and bandpasses.

analyses at 4.5 μm we found occultation depth differences on the order of 0.01% between our fits with a quadratic ramp and the selected ramp (Table 7). Another difference in the approaches is that Deming et al. (2023) analyzed the occultations individually, keeping the eclipse shape parameters fixed at values found in the literature. Instead, we obtained our final values from a joint fit of all occultations, where we simultaneously fit for the (shared) eclipse shape parameters. By sharing parameters in our joint-fit, we estimated the eclipse midpoint, duration and the time of ingress and egress with a precision comparable to that of the transit-shape parameters. Moreover, our eclipse values are consistent within 1σ of those expected from an orbit derived from the transit parameters assuming a circular orbit (see Tables 6 and 7). Comparing the 4.5 μm occultation depths between our individual and joint-fit analysis we see differences on the order of 0.002–0.005%. While admittedly speculative, given the limitations on the analysis details, occultation depth variations of this magnitude can bring the Deming et al. (2023) and our results closer to a 1σ agreement.

5. Results

5.1. Atmospheric modeling

To convert the observed eclipse depth into an estimate of the geometric albedo of a planet in a given passband it is important to quantify the flux thermally radiated by the planet at the same wavelengths. To this purpose, we performed various spectral retrievals of the *Spitzer* dataset, where the contribution from atmospheric reflection is negligible, with different model assumptions to determine a range of possible models compatible with the infrared observations. In this analysis, we exclude the eclipse depth measurement in the K_S band of Zhao et al. (2012) as it has been shown to be hardly reconciled to atmospheric models (Rostron et al. 2014).

To derive physically based priors for one retrieval run, we performed a forward model for WASP-3 b with the orbital and planetary parameters as listed in Table 1. For this purpose, we used the 3D general circulation model (GCM) `expeRT/MITgcm` (Carone et al. 2020; Schneider et al. 2022) with equilibrium chemistry. We chose the canonical opacity sources for a solar metallicity atmosphere as listed in Schneider et al. (2022, Table 1), including TiO. The dayside atmosphere composition of this simulation was used to constrain part of the retrieval pipeline, where we averaged the abundances over the whole dayside.

The retrieval models are defined using the TauREx code (Al-Refaie et al. 2021; Waldmann et al. 2015b,a), under different assumptions (from the simplest to the most complex one). The number of parameters defines the complexity of the model and, given the low number of input parameters (three wavelength points from the *Spitzer* dataset). We performed five different retrievals (we list them by increasing the number of parameters), changing the P–T (pressure vs temperature) profile and the chemical composition of the atmosphere:

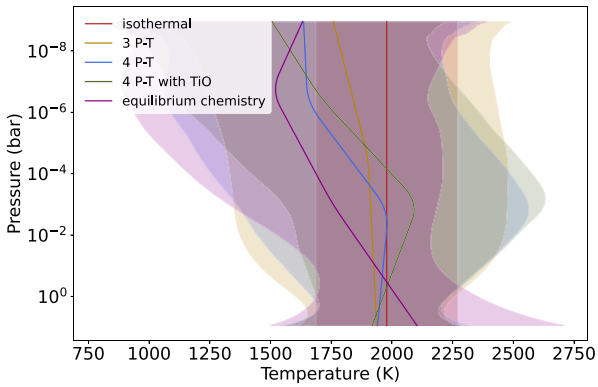

Fig. 6. Retrieved temperature-pressure profiles for all the atmospheric configurations.

1. Isothermal fit: We left only the radius and the equilibrium temperature as free parameters (two parameters);
2. 3PT: We fit three-point P-T profile and the radius (five free parameters). The atmosphere is assumed to be made only by H and He and solar abundances;
3. 4PT: We fit a four-point P-T profile and the radius (seven free parameters). We assumed the same chemistry of the 3PT model;
4. 4PT with TiO: We fit a four-point P-T profile and the radius fixing the TiO abundance as a function of the pressure from the 3D global circulation model (GCM) model (seven free parameters). We used the TiO opacities from the ExoMol group (Buldyreva et al. 2022);
5. 4PT with equilibrium chemistry: We fit a four-point P-T profile, the radius and the C/O ratio assuming equilibrium chemistry with FastChem (eight free parameters).

All the retrievals have been performed using Nested Sampling with the `multinest` (Feroz et al. 2009) through the `pymultinest` interface (Buchner et al. 2014) with 1000 live points and uniform prior distributions for all parameters. The atmospheric grid is defined between 10^{-4} Pa and 10^{6} Pa and, then the retrieved radius corresponds to the radius of the planet at 10^{6}Pa. We used the `phoenix` stellar model (Hauschildt et al. 1997, 1999) of WASP-3 for all the configurations.

The best-fit models for all these scenarios are shown in Fig. 5. The atmospheric models with the chemical species within them were computed using the cross sections from the ExoMol database (Tennyson et al. 2013, 2020)[6] while the equilibrium chemistry was computed with the FastChem[7] (Stock et al. 2022) through the `taurex-fastchem` plugin[8].

The temperature–pressure profiles retrieved with all the configurations are consistent with themselves (see Fig. 6). The presence of TiO causes a slight thermal inversion and it causes an increase in the optical thickness in the CHEOPS and TESS wavelength ranges as shown in Fig. 7, preventing sensitive optical band missions from probing low regions of the atmosphere. The level that can be probed with the different instruments is reported in Table 8.

All these models are equivalent from a statistical point of view: their Bayesian evidence $\log \mathcal{E}_{min} = 23.8$ for the case of the isothermal fit with two parameters while $\log \mathcal{E}_{max} = 24.4$ for the case of 4PT with FastChem. Given that the Bayes factor among any of the models is < 3, we cannot exclude any possibility in the computation of the thermal spectrum. Considering the Occam's principle, the simplest model gives already a solid understanding of the dayside brightness temperature $T_{\rm d} = 1980^{340}_{-240}$K and a radius $R_p = 1.25 \pm 0.19 R_{\rm Jup}$ (consistent with the radius reported in Table 6). We report all the thermal fluxes integrated into the CHEOPS and the TESS bandpass for all the scenarios in Table 9.

[6] https://www.exomol.com/data/molecules/
[7] https://ascl.net/1804.025
[8] https://pypi.org/project/taurex-fastchem

Table 8. Maximum contribution level (in bar) to the optical depth at the wavelength ranges of CHEOPS, TESS, and *Spitzer*.

Model	CHEOPS	TESS	*Spitzer*
Isothermal	8.9	8.9	1.32
3 P–T	7.12	8.2	0.6
4 P–T	8.9	8.9	1.76
4 P–T with TiO	$1.8 \cdot 10^{-5}$	$1.5 \cdot 10^{-5}$	1.39
4 P–T with eq. chemistry	0.15	0.27	$1.8 \cdot 10^{-2}$

Table 9. Simulated thermal fluxes on CHEOPS and TESS wavelength bands assuming different forward models. The error bars are computed from their 1σ distributions around the TauREx best-fit model.

Model	CHEOPS F_p/F_s (ppm)	TESS F_p/F_s (ppm)
Isothermal	2 ± 20	12 ± 47
3 P–T	1 ± 20	14 ± 53
4 P–T	4 ± 22	6 ± 60
4 P–T with TiO	0.2 ± 36	10 ± 80
4 P–T with eq. chemistry	17 ± 14	97 ± 38

5.2. Planetary albedo and heat recirculation

While the irradiation temperature $T_{\rm irr} = T_{\rm eff} \sqrt{R_\star/a}$ is a useful quantity to compare exoplanets because it only depends on the stellar irradiation, during secondary eclipse we measure the dayside effective temperature $T_{\rm d}$ that also factors in heat redistribution and albedo. The nominal thermal contribution to the CHEOPS and TESS eclipse depths is on the order of a few ppm regardless of the thermal model, with uncertainties on average of ~20 ppm for CHEOPS and ~60 ppm for TESS (Fig. 8, top panels). We subtracted these estimates to the measured eclipse depths and propagated the uncertainties in Eq. (1) to derive an unbiased estimate of the geometric albedo $A_{\rm g}$ of WASP-3 b (Fig. 8, bottom panels). The geometric albedo $A_{\rm g}^{\rm C}$ measured in the CHEOPS passband is ~0.21±0.07, while the uncertainties derived for the TESS passband do not allow a statistically significant measurement of the corresponding geometric albedos $A_{\rm g}^{\rm T}$; they only lead to a 95% upper limit of about 0.2. Our result thus follows the general trend of $A_{\rm g}$ increasing with $T_{\rm d}$ indicated by Wong et al. (2021) (Fig. 9).

The measurements in the case of TESS do not lead to a statistically significant measurement of $A_{\rm g}$. For this reason, in the following we only discuss the case of CHEOPS, dropping the "C" superscript for simplicity.

By definition, the geometric albedo $A_{\rm g}$ quantifies the incident light reflected back to the star at a given wavelength. The spherical albedo $A_{\rm S}$ is obtained from $A_{\rm g}$ by integration at all angles. The relationship between the two is parameterized by the phase integral q: $A_{\rm S} = qA_{\rm g}$ (see for example Seager 2010). Exoplanetary atmospheres have $1<q<1.5$ depending on their scattering law (Pollack et al. 1986; Burrows & Orton 2010) and can be

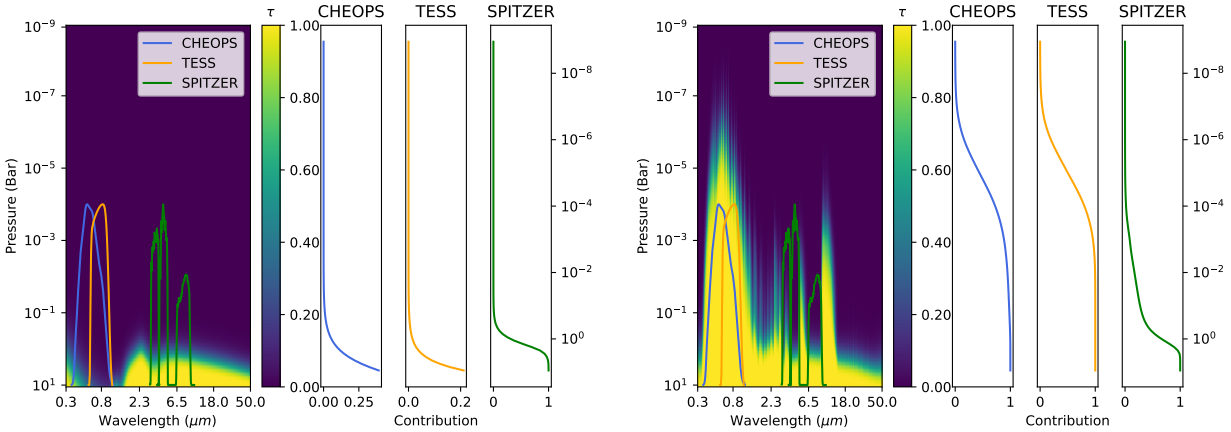

Fig. 7. Optical depth (τ) in the wavelength range of CHEOPS, TESS, and *Spitzer* space telescopes at every pressure level for the simulation labeled 4P-T (left) and 4 P–T with TiO (right). In the left panel of each figure is depicted the optical depth at each atmospheric pressure level. In the right panels there are the cumulative contribution functions at each atmospheric level for the CHEOPS, TESS and *Spitzer* space missions. In the presence of optical absorbers, CHEOPS and TESS can probe at a higher level than *Spitzer* compared to a case without optical absorbers.

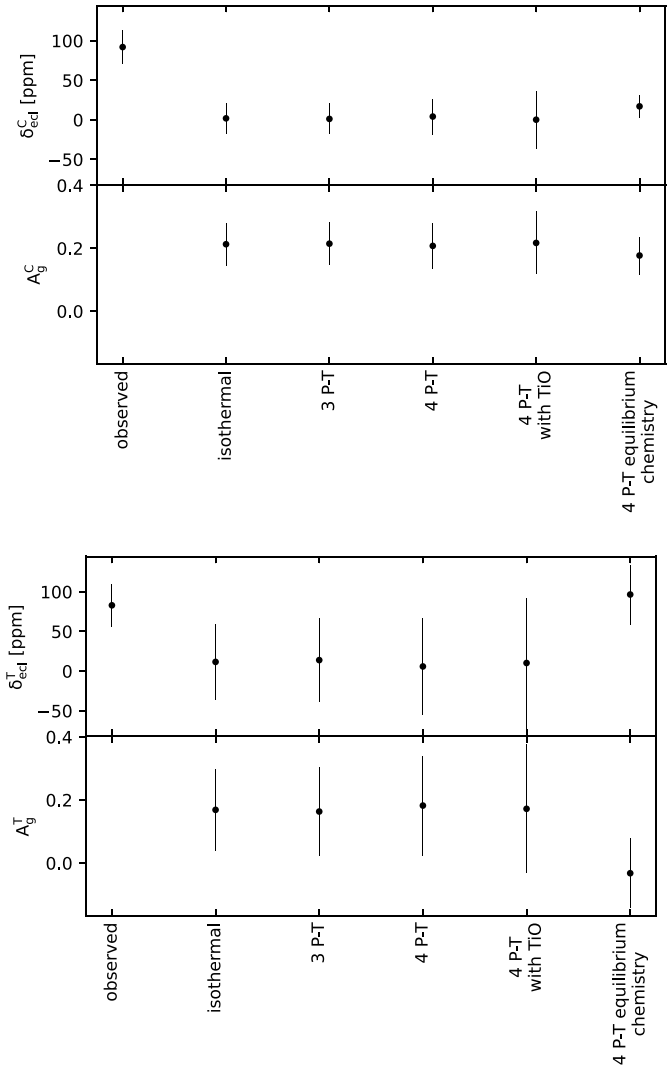

Fig. 8. Measured eclipse depth in the CHEOPS (δ^{C}_{ecl}, top panel) and TESS (δ^{T}_{ecl}, bottom panel) passbands together with the theoretical predictions discussed in the text. In each panel, the bottom boxes show the corresponding geometric albedos after correction for thermal emission.

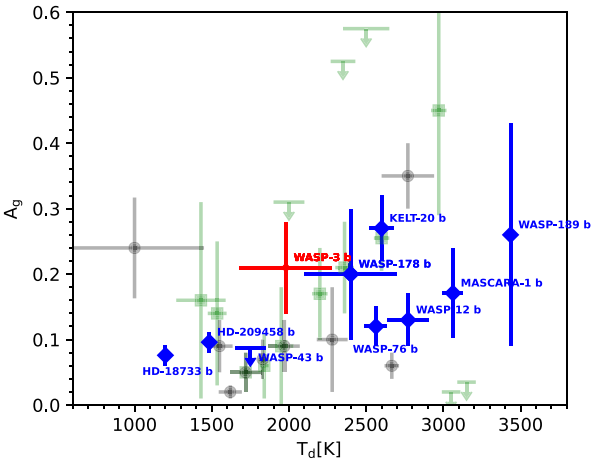

Fig. 9. Relationship between A_g and T_d, adapted from Fig. 10 in Wong et al. (2021) and including our analysis of WASP-3 b (in red). The green squares indicate the systems from the first and second year of the TESS primary mission. The black circles indicate the *Kepler*/CoRoT-band geometric albedos for the targets that were observed by those missions. Blue symbols are other targets from the CHEOPS GTO program (Lendl et al. 2020; Hooton et al. 2022; Brandeker et al. 2022; Singh et al. 2022; Scandariato et al. 2022; Krenn et al. 2023; Pagano et al. 2024; Akinsanmi et al. 2024; Demangeon et al. 2024).

observationally derived from the analysis of the phase curve. Unfortunately, no phase curve of WASP-3 b with enough precision is currently available, and hence we could not place any constraint on q. In the following we thus consider the two limiting scenarios $A_S^{min} = A_g$ and $A_S^{max} = 1.5A_g$.

The Bond albedo, A_B, can be obtained as the average of A_S weighted over the incident stellar spectrum:

$$A_B = \frac{\int_0^\infty A_S(\lambda) I_\star(\lambda) d\lambda}{\int_0^\infty I_\star(\lambda) d\lambda}. \quad (2)$$

The conversion into A_B thus relies on the measurement of A_S across the stellar spectrum, but we only have this information integrated in the CHEOPS passband. Following Schwartz & Cowan (2015), we explore the limit case of minimum Bond albedo A_B^{min} obtained through Eq. (2) assuming $A_S = A_S^{min}$ in the

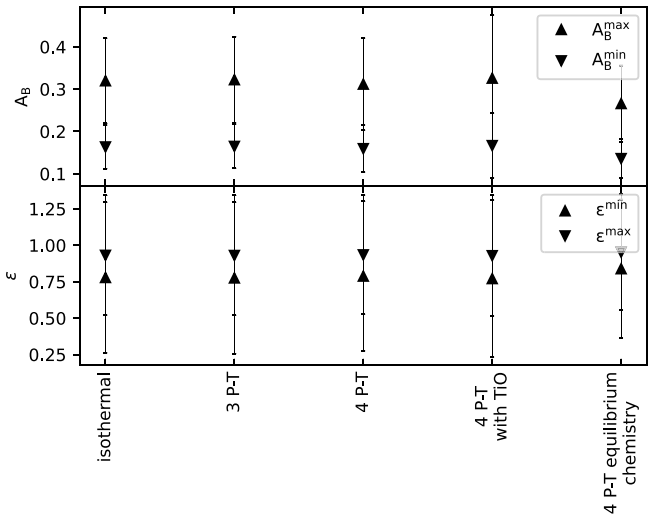

Fig. 10. Maximum and minimum Bond albedo, A_B, of WASP-3 b depending on the assumed thermal model (see the text) and corresponding minimum and maximum recirculation efficiency (top and bottom panel, respectively).

spectral range covered by CHEOPS and A_S =0 otherwise. The opposite limit case assumes $A_S(\lambda) = A_S^{max}$ at all wavelengths, which leads to $A_B^{max} = A_S^{max}$. To compute the integrals in Eq. (2), we used the synthetic spectrum in the BT-Settl library corresponding to the parameters of WASP-3 (Allard et al. 2012). Our results indicate that A_B has a weak dependence on the assumed atmospheric model: regardless of the scenario, A_B increases from ~0.16±0.06 to ~0.3±0.1 with increasing q (Fig. 10, top panel).

Cowan & Agol (2011) discuss a simple atmospheric energy budget and relate the dayside effective temperature, T_d, to the Bond albedo, A_B (the fraction of incident stellar light not absorbed by the planet) and the recirculation efficiency, ϵ (the homogeneity by which the absorbed stellar energy is distributed across the planetary surface):

$$T_d = T_{eff}\sqrt{\frac{R_\star}{a}}(1-A_B)^{1/4}\left(\frac{2}{3}-\frac{5}{12}\epsilon\right)^{1/4}. \quad (3)$$

Inverting Eq. (3) yields

$$\epsilon = \frac{1}{5}\left[8-\left(\frac{T_d}{T_{eff}}\right)^4\left(\frac{a}{R_\star}\right)^2\frac{12}{1-A_B}\right]. \quad (4)$$

Equation (4) indicates that ϵ decreases as A_B increases. This is due to the fact that for a fixed T_d the model allows for a more efficient energy recirculation from day- to nightside (higher ϵ) when more incident stellar light is absorbed by the atmosphere (low A_B). Plugging in the T_d and A_B estimates discussed above and propagating the corresponding uncertainties we derived that the assumptions of minimum and maximum A_S lead to ϵ predictions compared with the 1σ uncertainties (Fig. 10).

Figure 10 also shows that the ϵ estimates according to different thermal models are all consistent with each other; the differences are much smaller than the 1σ uncertainties. They all agree in indicating an almost complete energy recirculation ($\epsilon \lesssim 1$). This result would lead to a perfectly isothermal planetary surface, an unrealistic scenario that we discuss in Sect. 6.

6. Discussion and conclusion

With the aim of characterizing the climate of the HJ WASP-3 b, in this paper we have analyzed the CHEOPS, TESS, and *Spitzer* photometry of the secondary eclipses of the planet. We find that the planetary atmosphere has a maximum Bond albedo of 0.3±0.1 and likely has an efficient energy redistribution. WASP-3 b is thus as reflective as similar ultra-hot Jupiters (UHJs) but does not fit the general expectation of low ϵ proposed by Cowan & Agol (2011).

From a theoretical perspective, the temperature contrast between the day- and nightside of HJs is governed by the presence of strong advective latitudinal winds in the planetary atmospheres (Komacek & Showman 2016, and references therein). The efficiency by which energy is redistributed from the day- to the nightside decreases as T_{irr} increases (see Table 6) because the timescale of irradiation becomes shorter than the advective timescale (see also Perez-Becker & Showman 2013; Schwartz et al. 2017; Parmentier & Crossfield 2018; Baeyens et al. 2021). More specifically, the day–night temperature contrast is highest for ultra-hot planets with $T_{irr} \geq 2000$ K (Helling et al. 2023). Accordingly, WASP-3 b is in the ultra-hot temperature regime where heat recirculation is expected to be low, in contrast with our finding.

Similarly, Zhang et al. (2018) and May et al. (2021) collected observational evidence that the phase curves' offset of HJs decreases with increasing T_{irr}. This results hints to the presence of zonal winds that make the redistribution of the energy less efficient in the atmosphere of highly irradiated HJs like WASP-3 b.

Furthermore, for UHJs similar to WASP-3 b, a clear dayside that is too hot for cloud formation and a cloudy nightside is predicted from 3D climate models (e.g., Helling et al. 2019b, 2023; Roman et al. 2021; Parmentier et al. 2021). The backwarming effect due to clouds will warm up the nightside and thus reduce the day-to-nightside temperature gradient, reducing the horizontal wind speeds and thus the efficiency of horizontal heat transfer even more (Roman et al. 2021; Parmentier et al. 2021). Roman et al. (2021) predict low day side albedos, ≤0.15, consistent with our findings on WASP-3 b.

Theoretical predictions from 3D climate models and observed phase curve offsets consistently suggest that highly irradiated UHJs like WASP-3 b should be characterized by low values of the recirculation efficiency, ϵ. Conversely, our analysis suggests that the atmosphere of WASP-3 b efficiently redistributes energy from the dayside to the nightside, leaving the possibility that mechanisms for energy redistribution other than advective winds are at play. One possibility that has emerged in the last years is that for planets with $T_{irr} \geq 2500$ K the temperature of the dayside is high enough to dissociate the H_2 molecules. This ionized gas then recombines, crossing the limbs and reaching the nightside, where lower temperatures enable molecular recombination and the consequent energy release. This scenario is supported by several studies (Bell & Cowan 2018; Tan & Komacek 2019; Mansfield et al. 2020; Helling et al. 2021, 2023) and is consistent with the irradiation temperature of WASP-3 b (Table 4).

The conundrum of a large recirculation efficiency can be an artifact of either the model depicted in Eqs. (3)–(4) or our assumed physical parameters. For example, ϵ has a strong dependence on the brightness temperature: by assuming a higher T_d of 2400 K (statistically consistent within 2σ with the estimate discussed in Sect. 5.1), ϵ decreases to a lower value of ~0.4, with an uncertainty that makes it consistent with 0 within 1σ.

One possible explanation for our underestimation of the dayside brightness temperature is the presence of optical absorbers in the atmosphere of WASP-3 b. For example, in Fig. 7 we show that if TiO is present in the atmosphere, then CHEOPS and TESS probe higher and hotter atmospheric layers than *Spitzer*. This can potentially increase T_d enough to reconcile ϵ with the expectations. Recently, Roth et al. (2024) revisited the question of TiO cold-trapping from the gas phase in HJs (Parmentier et al. 2013). These authors predict that there is a transition at T_{eq} = 1800 K from HJs with low abundances of TiO in the gas phase toward UHJs with significant abundances of TiO. A transition in dayside brightness at 1800 K was also inferred from a statistical analysis of a *Spitzer* eclipse observation (Deming et al. 2023). The slight thermal inversion inferred from atmosphere retrieval appears to confirm that WASP-3 b lies in a transition region where TiO abundances may be affected by cloud formation. However, neither Roth et al. (2024) nor Deming et al. (2023) performed microphysical modeling that studies the TiO abundances affected by cloud formation. Microphysical cloud models like DRIFT (e.g., Helling & Woitke 2006) provide further insight. Helling et al. (2023, Fig. 15) and Helling et al. (2019a, Fig. A12) demonstrate that the TiO abundances are substantially affected by condensation processes into, for example, TiO_2, which can indeed occur on the dayside of planets in this temperature transition region. At the same time, aerosols of highly diverse compositions can form in the upper atmosphere and reduce the oxygen abundance – if the temperature is cold enough to allow a thermal stability of these particles. If TiO is abundant enough to force a strong upper atmosphere temperature inversion on the dayside of a HJ, then the resulting high temperatures inhibit aerosol formation (Helling et al. 2023, Fig. 15). Thus, the formation of upper atmosphere temperature inversions, TiO abundances, and the absence or presence of high-altitude aerosols go hand in hand. Answering the question of whether aerosols form on the dayside of WASP-3 b and contribute to the observed albedo, however, requires a dedicated microphysical nucleation model and better constraints of the TiO abundances for this planet. In any case, WASP-3 b is a highly interesting target for further in-depth characterization to address, for example, TiO nucleation, cloud dissipation, and the nature of high-altitude aerosols on the dayside of HJs.

Moreover, under the assumption of different instruments probing different atmospheric layers, to have a comprehensive view, it is necessary to model how the physical and chemical conditions vary with atmospheric height. This dependence can potentially disprove the assumptions of the analytic model proposed by Cowan & Agol (2011). In this regard, the unexpected high ϵ could be an artifact from adapting a simple atmospheric model to a stratified atmosphere where complex processes are at play. In conclusion, WASP-3 b is an interesting test case for more in-depth future investigations aimed at validating and constraining current atmospheric models for UHJs.

Data availability

The light curves, ancillary data and spacecraft housekeeping data generated from the CHEOPS observations of WASP-3 by the PIPE PSF-fitting photometry package are available in electronic form at the CDS via anonymous ftp to cdsarc.cds.unistra.fr (130.79.128.5) or via https://cdsarc.cds.unistra.fr/viz-bin/cat/J/A+A/692/A129. The TESS observations of WASP-3 can be obtained from the Mikulski Archive for Space Telescopes data archive at the Space Telescope Science Institute (STScI) (https://archive.stsci.edu). The Spitzer observations of WASP-3 used in this analysis are available from the Spitzer Heritage Archive (DOI:https://doi.org/10.26131/IRSA543) held at the NASA/IPAC Infrared Science Archive (https://irsa.ipac.caltech.edu/).

Acknowledgements. CHEOPS is an ESA mission in partnership with Switzerland with important contributions to the payload and the ground segment from Austria, Belgium, France, Germany, Hungary, Italy, Portugal, Spain, Sweden, and the United Kingdom. The CHEOPS Consortium would like to gratefully acknowledge the support received by all the agencies, offices, universities, and industries involved. Their flexibility and willingness to explore new approaches were essential to the success of this mission. CHEOPS data analyzed in this article will be made available in the CHEOPS mission archive (https://cheops.unige.ch/archive_browser/). GSc and CSt acknowledge the long waited "Mã" project and are speechlessly thankful to all the colleagues who have wonderfully run the project so far on their behalf (ACa, MLu and co-workers). LBo, GBr, VNa, IPa, GPi, RRa, GSc, VSi, and TZi acknowledge support from CHEOPS ASI-INAF agreement n. 2019-29-HH.0. LCa and ChH acknowledge the European Union H2020-MSCA-ITN-2019 under Grant Agreement no. 860470 (CHAMELEON), and the HPC facilities of the Vienna Science Cluster (VSC project 72245). P.E.C. is funded by the Austrian Science Fund (FWF) Erwin Schroedinger Fellowship, program J4595-N. PM acknowledges support from STFC research grant number ST/R000638/1. TZi acknowledges NVIDIA Academic Hardware Grant Program for the use of the Titan V GPU card and the Italian MUR Departments of Excellence grant 2023–2027 "Quantum Frontiers". MNG is the ESA CHEOPS Project Scientist and Mission Representative, and as such also responsible for the Guest Observers (GO) Programme. MNG does not relay proprietary information between the GO and Guaranteed Time Observation (GTO) Programmes, and does not decide on the definition and target selection of the GTO Programme. ML acknowledges support of the Swiss National Science Foundation under grant number PCEFP2_194576. TWi acknowledges support from the UKSA and the University of Warwick. YAl acknowledges support from the Swiss National Science Foundation (SNSF) under grant 200020_192038. We acknowledge financial support from the Agencia Estatal de Investigación of the Ministerio de Ciencia e Innovación MCIN/AEI/10.13039/501100011033 and the ERDF "A way of making Europe" through projects PID2019-107061GB-C61, PID2019-107061GB-C66, PID2021-125627OB-C31, and PID2021-125627OB-C32, from the Centre of Excellence "Severo Ochoa" award to the Instituto de Astrofísica de Canarias (CEX2019-000920-S), from the Centre of Excellence "María de Maeztu" award to the Institut de Ciències de l'Espai (CEX2020-001058-M), and from the Generalitat de Catalunya/CERCA programme. We acknowledge financial support from the Agencia Estatal de Investigación of the Ministerio de Ciencia e Innovación MCIN/AEI/10.13039/501100011033 and the ERDF "A way of making Europe" through projects PID2019-107061GB-C61, PID2019-107061GB-C66, PID2021-125627OB-C31, and PID2021-125627OB-C32, from the Centre of Excellence "Severo Ochoa" award to the Instituto de Astrofísica de Canarias (CEX2019-000920-S), from the Centre of Excellence "María de Maeztu" award to the Institut de Ciències de l'Espai (CEX2020-001058-M), and from the Generalitat de Catalunya/CERCA programme. S.C.C.B. acknowledges support from FCT through FCT contracts nr. IF/01312/2014/CP1215/CT0004. ABr was supported by the SNSA. C.B. acknowledges support from the Swiss Space Office through the ESA PRODEX program. This work has been carried out within the framework of the NCCR PlanetS supported by the Swiss National Science Foundation under grants 51NF40_182901 and 51NF40_205606. ACC acknowledges support from STFC consolidated grant number ST/V000861/1, and UKSA grant number ST/X002217/1. ACMC acknowledges support from the FCT, Portugal, through the CFisUC projects UIDB/04564/2020 and UIDP/04564/2020, with DOI identifiers 10.54499/UIDB/04564/2020 and 10.54499/UIDP/04564/2020, respectively. A.C., A.D., B.E., K.G., and J.K. acknowledge their role as ESA-appointed CHEOPS Science Team Members. This project was supported by the CNES. The Belgian participation to CHEOPS has been supported by the Belgian Federal Science Policy Office (BELSPO) in the framework of the PRODEX Program, and by the University of Liège through an ARC grant for Concerted Research Actions financed by the Wallonia-Brussels Federation. L.D. thanks the Belgian Federal Science Policy Office (BELSPO) for the provision of financial support in the framework of the PRODEX Programme of the European Space Agency (ESA) under contract number 4000142531. This work was supported by FCT – Fundação para a Ciência e a Tecnologia through national funds and by FEDER through COMPETE2020 through the research grants UIDB/04434/2020, UIDP/04434/2020, 2022.06962.PTDC. O.D.S.D. is supported in the form of work contract (DL 57/2016/CP1364/CT0004) funded by national funds through FCT. B.-O.D. acknowledges support from the Swiss State Secretariat for Education, Research and Innovation (SERI) under contract number MB22.00046. This project has received funding from the Swiss National Science Foundation for project 200021_200726. It has also been carried out within

the framework of the National Centre of Competence in Research PlanetS supported by the Swiss National Science Foundation under grant 51NF40_205606. The authors acknowledge the financial support of the SNSF. MF and CMP gratefully acknowledge the support of the Swedish National Space Agency (DNR 65/19, 174/18). DG gratefully acknowledges financial support from the CRT foundation under Grant No. 2018.2323 "Gaseousor rocky? Unveiling the nature of small worlds". M.G. is an F.R.S.-FNRS Senior Research Associate. CHe acknowledges support from the European Union H2020-MSCA-ITN-2019 under Grant Agreement no. 860470 (CHAMELEON). KGI is the ESA CHEOPS Project Scientist and is responsible for the ESA CHEOPS Guest Observers Programme. She does not participate in, or contribute to, the definition of the Guaranteed Time Programme of the CHEOPS mission through which observations described in this paper have been taken, nor to any aspect of target selection for the programme. K.W.F.L. was supported by Deutsche Forschungsgemeinschaft grants RA714/14-1 within the DFG Schwerpunkt SPP 1992, Exploring the Diversity of Extrasolar Planets. This work was granted access to the HPC resources of MesoPSL financed by the Region Ile de France and the project Equip@Meso (reference ANR-10-EQPX-29-01) of the programme Investissements d'Avenir supervised by the Agence Nationale pour la Recherche. This work was also partially supported by a grant from the Simons Foundation (PI Queloz, grant number 327127). NCSa acknowledges funding by the European Union (ERC, FIERCE, 101052347). Views and opinions expressed are however those of the author(s) only and do not necessarily reflect those of the European Union or the European Research Council. Neither the European Union nor the granting authority can be held responsible for them. A. S. acknowledges support from the Swiss Space Office through the ESA PRODEX program. S.G.S. acknowledge support from FCT through FCT contract nr. CEECIND/00826/2018 and POPH/FSE (EC). The Portuguese team thanks the Portuguese Space Agency for the provision of financial support in the framework of the PRODEX Programme of the European Space Agency (ESA) under contract number 4000142255. GyMSz acknowledges the support of the Hungarian National Research, Development and Innovation Office (NKFIH) grant K-125015, a PRODEX Experiment Agreement No. 4000137122, the Lendület LP2018-7/2021 grant of the Hungarian Academy of Science and the support of the city of Szombathely. V.V.G. is an F.R.S-FNRS Research Associate. JV acknowledges support from the Swiss National Science Foundation (SNSF) under grant PZ00P2_208945. NAW acknowledges UKSA grant ST/R004838/1. E.V. acknowledges support from the 'DISCOBOLO' project funded by the Spanish Ministerio de Ciencia, Innovación y Universidades under grant PID2021-127289NB-I00. This research has made use of the NASA/IPAC Infrared Science Archive, which is funded by the National Aeronautics and Space Administration and operated by the California Institute of Technology. This paper includes data collected by the TESS mission. Funding for the TESS mission is provided by the NASA's Science Mission Directorate.

References

Akinsanmi, B., Barros, S. C. C., Lendl, M., et al. 2024, A&A, 685, A63
Al-Refaie, A. F., Changeat, Q., Waldmann, I. P., & Tinetti, G. 2021, ApJ, 917, 37
Allan, D. W. 1966, IEEE Proc., 54, 221
Allard, F., Homeier, D., & Freytag, B. 2012, Philos. Trans. Roy. Soc. Lond. A, 370, 2765
Baeyens, R., Decin, L., Carone, L., et al. 2021, MNRAS, 505, 5603
Bell, T. J., & Cowan, N. B. 2018, ApJ, 857, L20
Benz, W., Broeg, C., Fortier, A., et al. 2021, Ex. Astron., 51, 109
Blackwell, D. E., & Shallis, M. J. 1977, MNRAS, 180, 177
Bonfanti, A., Ortolani, S., Piotto, G., & Nascimbeni, V. 2015, A&A, 575, A18
Bonfanti, A., Ortolani, S., & Nascimbeni, V. 2016, A&A, 585, A5
Bonfanti, A., Delrez, L., Hooton, M. J., et al. 2021, A&A, 646, A157
Bonomo, A. S., Desidera, S., Benatti, S., et al. 2017, A&A, 602, A107
Brandeker, A., Heng, K., Lendl, M., et al. 2022, A&A, 659, L4
Buchner, J., Georgakakis, A., Nandra, K., et al. 2014, A&A, 564, A125
Buldyreva, J., Yurchenko, S. N., & Tennyson, J. 2022, RAS Tech. Instrum., 1, 43
Burrows, A., & Orton, G. 2010, in Exoplanets, ed. S. Seager, 419
Campo, C. J., Harrington, J., Hardy, R. A., et al. 2011, ApJ, 727, 125
Carone, L., Baeyens, R., Mollière, P., et al. 2020, MNRAS, 496, 3582
Castelli, F., & Kurucz, R. L. 2003, in IAU Symposium, 210, Modelling of Stellar Atmospheres, eds. N. Piskunov, W. W. Weiss, & D. F. Gray, A20
Charbonneau, D., Allen, L. E., Megeath, S. T., et al. 2005, ApJ, 626, 523
Collier Cameron, A., Ford, E. B., Shahaf, S., et al. 2021, MNRAS, 505, 1699
Cowan, N. B., & Agol, E. 2011, ApJ, 729, 54
Cubillos, P., Harrington, J., Madhusudhan, N., et al. 2013, ApJ, 768, 42
Cubillos, P., Harrington, J., Madhusudhan, N., et al. 2014, ApJ, 797, 42
Cubillos, P., Harrington, J., Loredo, T. J., et al. 2017, AJ, 153, 3
Demangeon, O. D. S., Cubillos, P. E., Singh, V., et al. 2024, A&A, 684, A27
Deming, D., Knutson, H., Kammer, J., et al. 2015, ApJ, 805, 132
Deming, D., Line, M. R., Knutson, H. A., et al. 2023, AJ, 165, 104
Fazio, G. G., Hora, J. L., Allen, L. E., et al. 2004, ApJS, 154, 10
Feroz, F., Hobson, M. P., & Bridges, M. 2009, MNRAS, 398, 1601
Foreman-Mackey, D., Hogg, D. W., Lang, D., & Goodman, J. 2013, PASP, 125, 306
Fortier, A., Simon, A. E., Broeg, C., et al. 2024, A&A, 687, A302
Fortney, J. J., Dawson, R. I., & Komacek, T. D. 2021, J. Geophys. Res. Planets, 126, e06629
Gaia Collaboration (Vallenari, A., et al.) 2023, A&A, 674, A1
Gelman, A., & Rubin, D. B. 1992, Statist. Sci., 7, 457
Hauschildt, P. H., Baron, E., & Allard, F. 1997, ApJ, 483, 390
Hauschildt, P. H., Allard, F., & Baron, E. 1999, ApJ, 512, 377
Helling, C., & Woitke, P. 2006, A&A, 455, 325
Helling, C., Gourbin, P., Woitke, P., & Parmentier, V. 2019a, A&A, 626, A133
Helling, C., Iro, N., Corrales, L., et al. 2019b, A&A, 631, A79
Helling, C., Worters, M., Samra, D., Molaverdikhani, K., & Iro, N. 2021, A&A, 648, A80
Helling, C., Samra, D., Lewis, D., et al. 2023, A&A, 671, A122
Heng, K. 2017, Exoplanetary Atmospheres: Theoretical Concepts and Foundations (Princeton University Press)
Høg, E., Fabricius, C., Makarov, V. V., et al. 2000, A&A, 355, L27
Hooton, M. J., Hoyer, S., Kitzmann, D., et al. 2022, A&A, 658, A75
Hoyer, S., Guterman, P., Demangeon, O., et al. 2020, A&A, 635, A24
Hoyer, S., Jenkins, J. S., Parmentier, V., et al. 2023, A&A, 675, A81
Ingalls, J. G., Krick, J. E., Carey, S. J., et al. 2016, AJ, 152, 44
Komacek, T. D., & Showman, A. P. 2016, ApJ, 821, 16
Krenn, A. F., Lendl, M., Patel, J. A., et al. 2023, A&A, 672, A24
Léger, A., Rouan, D., Schneider, J., et al. 2009, A&A, 506, 287
Lendl, M., Csizmadia, S., Deline, A., et al. 2020, A&A, 643, A94
Lightkurve Collaboration (Cardoso, J. V. d. M., et al.) 2018, Lightkurve: Kepler and TESS time series analysis in Python, Astrophysics Source Code Library [record ascl:1812.013]
Lindegren, L., Bastian, U., Biermann, M., et al. 2021, A&A, 649, A4
Maciejewski, G., Niedzielski, A., Wolszczan, A., et al. 2013, AJ, 146, 147
Mandel, K., & Agol, E. 2002, ApJ, 580, L171
Mansfield, M., Bean, J. L., Stevenson, K. B., et al. 2020, ApJ, 888, L15
Marigo, P., Girardi, L., Bressan, A., et al. 2017, ApJ, 835, 77
Maxted, P. F. L. 2018, A&A, 616, A39
Maxted, P. F. L., & Gill, S. 2019, A&A, 622, A33
Maxted, P. F. L., Ehrenreich, D., Wilson, T. G., et al. 2022, MNRAS, 514, 77
May, E. M., Komacek, T. D., Stevenson, K. B., et al. 2021, AJ, 162, 158
Montalto, M., Gregorio, J., Boué, G., et al. 2012, MNRAS, 427, 2757
Morris, B. M., Heng, K., Brandeker, A., Swan, A., & Lendl, M. 2021, A&A, 651, L12
Nymeyer, S., Harrington, J., Hardy, R. A., et al. 2011, ApJ, 742, 35
Oddo, D., Dragomir, D., Brandeker, A., et al. 2023, AJ, 165, 134
Pagano, I., Scandariato, G., Singh, V., et al. 2024, A&A, 682, A102
Parmentier, V. & Crossfield, I. J. M. 2018, in Handbook of Exoplanets, eds. H. J. Deeg & J. A. Belmonte, 116
Parmentier, V., Showman, A. P., & Lian, Y. 2013, A&A, 558, A91
Parmentier, V., Showman, A. P., & Fortney, J. J. 2021, MNRAS, 501, 78
Parviainen, H., Wilson, T. G., Lendl, M., et al. 2022, A&A, 668, A93
Perez-Becker, D., & Showman, A. P. 2013, ApJ, 776, 134
Perryman, M. 2011, The Exoplanet Handbook (New York: Cambridge University Press)
Pollacco, D., Skillen, I., Collier Cameron, A., et al. 2008, MNRAS, 385, 1576
Pollack, J. B., Podolak, M., Bodenheimer, P., & Christofferson, B. 1986, Icarus, 67, 409
Ricker, G. R., Winn, J. N., Vanderspek, R., et al. 2015, J. Astron. Telesc. Instrum. Syst., 1, 014003
Roman, M. T., Kempton, E. M. R., Rauscher, E., et al. 2021, ApJ, 908, 101
Rostron, J. W., Wheatley, P. J., Anderson, D. R., et al. 2014, MNRAS, 441, 3666
Roth, A., Parmentier, V., & Hammond, M. 2024, MNRAS, 531, 1056
Scandariato, G., Singh, V., Kitzmann, D., et al. 2022, A&A, 668, A17
Schanche, N., Hébrard, G., Collier Cameron, A., et al. 2020, MNRAS, 499, 428
Schneider, A. D., Carone, L., Decin, L., et al. 2022, A&A, 664, A56
Schwarz, G. 1978, Ann. Statist., 6, 461
Schwartz, J. C., & Cowan, N. B. 2015, MNRAS, 449, 4192
Schwartz, J. C., Kashner, Z., Jovmir, D., & Cowan, N. B. 2017, ApJ, 850, 154
Scuflaire, R., Théado, S., Montalbán, J., et al. 2008, Ap&SS, 316, 83
Seager, S. 2010, Exoplanet Atmospheres: Physical Processes (Princeton University Press)
Seager, S., & Dotson, R. 2010, Exoplanets, Space Science Series (University of Arizona Press)
Siegel, A. 1982, Biometrika, 69, 242
Singh, V., Bonomo, A. S., Scandariato, G., et al. 2022, A&A, 658, A132
Skrutskie, M. F., Cutri, R. M., Stiening, R., et al. 2006, AJ, 131, 1163
Stevenson, K. B., Harrington, J., Nymeyer, S., et al. 2010, Nature, 464, 1161
Stevenson, K. B., Harrington, J., Fortney, J. J., et al. 2012a, ApJ, 754, 136
Stevenson, K. B., Harrington, J., Lust, N. B., et al. 2012b, ApJ, 755, 9

Stock, J. W., Kitzmann, D., & Patzer, A. B. C. 2022, MNRAS, 517, 4070
Street, R. A., Christian, D. J., Clarkson, W. I., et al. 2007, MNRAS, 379, 816
Sudarsky, D., Burrows, A., & Pinto, P. 2000, ApJ, 538, 885
Sulis, S., Lendl, M., Cegla, H. M., et al. 2023, A&A, 670, A24
Szabó, G. M., Gandolfi, D., Brandeker, A., et al. 2021, A&A, 654, A159
Tan, X., & Komacek, T. D. 2019, ApJ, 886, 26
Tennyson, J., Hill, C., & Yurchenko, S. N. 2013, AIP Conf. Ser., 1545, 186
Tennyson, J., Yurchenko, S. N., Al-Refaie, A. F., et al. 2020, J. Quant. Spec. Radiat. Transf., 255, 107228
ter Braak, C. J. F., & Vrugt, J. A. 2008, Statist. Comput., 18, 435
Waldmann, I. P., Rocchetto, M., Tinetti, G., et al. 2015a, ApJ, 813, 13
Waldmann, I. P., Tinetti, G., Rocchetto, M., et al. 2015b, ApJ, 802, 107
Wilson, T. G., Goffo, E., Alibert, Y., et al. 2022, MNRAS, 511, 1043
Wong, I., Kitzmann, D., Shporer, A., et al. 2021, AJ, 162, 127
Wright, E. L., Eisenhardt, P. R. M., Mainzer, A. K., et al. 2010, AJ, 140, 1868
Zhang, M., Knutson, H. A., Kataria, T., et al. 2018, AJ, 155, 83
Zhao, M., Monnier, J. D., Swain, M. R., Barman, T., & Hinkley, S. 2012, ApJ, 744, 122

[1] INAF, Osservatorio Astrofisico di Catania, Via S. Sofia 78, 95123 Catania, Italy
[2] Space Research Institute, Austrian Academy of Sciences, Schmiedlstrasse 6, 8042 Graz, Austria
[3] INAF, Osservatorio Astrofisico di Torino, Via Osservatorio, 20, 10025 Pino Torinese To, Italy
[4] Astrophysics Group, Lennard Jones Building, Keele University, Staffordshire, ST5 5BG, UK
[5] Dipartimento di Fisica e Astronomia "Galileo Galilei", Università degli Studi di Padova, Vicolo dell'Osservatorio 3, 35122 Padova, Italy
[6] INAF, Osservatorio Astronomico di Padova, Vicolo dell'Osservatorio 5, 35122 Padova, Italy
[7] European Space Agency (ESA), European Space Research and Technology Centre (ESTEC), Keplerlaan 1, 2201 AZ Noordwijk, The Netherlands
[8] Observatoire astronomique de l'Université de Genève, Chemin Pegasi 51, 1290 Versoix, Switzerland
[9] Department of Physics, University of Warwick, Gibbet Hill Road, Coventry CV4 7AL, UK
[10] Center for Space and Habitability, University of Bern, Gesellschaftsstrasse 6, 3012 Bern, Switzerland
[11] SUPA, School of Physics and Astronomy, Kelvin Building, University of Glasgow, Glasgow, G12 8QQ, Scotland, UK
[12] Weltraumforschung und Planetologie, Physikalisches Institut, University of Bern, Gesellschaftsstrasse 6, 3012 Bern, Switzerland
[13] Instituto de Astrofísica de Canarias, Vía Láctea s/n, 38200 La Laguna, Tenerife, Spain
[14] Departamento de Astrofísica, Universidad de La Laguna, Astrofísico Francisco Sanchez s/n, 38206 La Laguna, Tenerife, Spain
[15] Admatis, 5. Kandó Kálmán Street, 3534 Miskolc, Hungary
[16] Depto. de Astrofísica, Centro de Astrobiología (CSIC-INTA), ESAC campus, 28692 Villanueva de la Cañada (Madrid), Spain
[17] Instituto de Astrofisica e Ciencias do Espaco, Universidade do Porto, CAUP, Rua das Estrelas, 4150-762 Porto, Portugal
[18] Departamento de Fisica e Astronomia, Faculdade de Ciencias, Universidade do Porto, Rua do Campo Alegre, 4169-007 Porto, Portugal
[19] Department of Astronomy, Stockholm University, AlbaNova University Center, 10691 Stockholm, Sweden
[20] Institute of Optical Sensor Systems, German Aerospace Center (DLR), Rutherfordstrasse 2, 12489 Berlin, Germany
[21] Space Research and Planetology, University of Bern, Gesellschaftsstrasse 6, 3012 Bern, Switzerland
[22] Centre for Exoplanet Science, SUPA School of Physics and Astronomy, University of St Andrews, North Haugh, St Andrews KY16 9SS, UK
[23] CFisUC, Departamento de Física, Universidade de Coimbra, 3004-516 Coimbra, Portugal
[24] Institute of Planetary Research, German Aerospace Center (DLR), Rutherfordstrasse 2, 12489 Berlin, Germany
[25] Centre for Mathematical Sciences, Lund University, Box 118, 221 00 Lund, Sweden
[26] Aix-Marseille Univ., CNRS, CNES, LAM, 38 rue Frédéric Joliot-Curie, 13388 Marseille, France
[27] Astrobiology Research Unit, Université de Liège, Allée du 6 Août 19C, 4000 Liège, Belgium
[28] Space sciences, Technologies and Astrophysics Research (STAR) Institute, Université de Liège, Allée du 6 Août 19C, 4000 Liège, Belgium
[29] Institute of Astronomy, KU Leuven, Celestijnenlaan 200D, 3001 Leuven, Belgium
[30] ELTE Gothard Astrophysical Observatory, 9700 Szombathely, Szent Imre h. u. 112, Hungary
[31] SRON Netherlands Institute for Space Research, Niels Bohrweg 4, 2333 CA Leiden, The Netherlands
[32] Centre Vie dans l'Univers, Faculté des sciences, Université de Genève, Quai Ernest-Ansermet 30, 1211 Genève 4, Switzerland
[33] Leiden Observatory, University of Leiden, PO Box 9513, 2300 RA Leiden, The Netherlands
[34] Department of Space, Earth and Environment, Chalmers University of Technology, Onsala Space Observatory, 439 92 Onsala, Sweden
[35] Dipartimento di Fisica, Università degli Studi di Torino, via Pietro Giuria 1, 10125, Torino, Italy
[36] National and Kapodistrian University of Athens, Department of Physics, University Campus, Zografos 157 84, Athens, Greece
[37] Department of Astrophysics, University of Vienna, Türkenschanzstrasse 17, 1180 Vienna, Austria
[38] Institute for Theoretical Physics and Computational Physics, Graz University of Technology, Petersgasse 16, 8010 Graz, Austria
[39] Konkoly Observatory, Research Centre for Astronomy and Earth Sciences, 1121 Budapest, Konkoly Thege Miklós út 15–17, Hungary
[40] ELTE Eötvös Loránd University, Institute of Physics, Pázmány Péter sétány 1/A, 1117 Budapest, Hungary
[41] Lund Observatory, Division of Astrophysics, Department of Physics, Lund University, Box 118, 22100 Lund, Sweden
[42] IMCCE, UMR8028 CNRS, Observatoire de Paris, PSL Univ., Sorbonne Univ., 77 av. Denfert-Rochereau, 75014 Paris, France
[43] Institut d'astrophysique de Paris, UMR7095 CNRS, Université Pierre & Marie Curie, 98bis bd. Arago, 75014 Paris, France
[44] European Space Agency, ESA – European Space Astronomy Centre, Camino Bajo del Castillo s/n, 28692 Villanueva de la Cañada, Madrid, Spain
[45] ETH Zurich, Department of Physics, Wolfgang-Pauli-Strasse 2, CH-8093 Zurich, Switzerland
[46] Cavendish Laboratory, JJ Thomson Avenue, Cambridge CB3 0HE, UK
[47] Institut fuer Geologische Wissenschaften, Freie Universitaet Berlin, Maltheserstrasse 74-100, 12249 Berlin, Germany
[48] Institut de Ciencies de l'Espai (ICE, CSIC), Campus UAB, Can Magrans s/n, 08193 Bellaterra, Spain
[49] Institut d'Estudis Espacials de Catalunya (IEEC), 08860 Castelldefels (Barcelona), Spain
[50] HUN-REN-ELTE Exoplanet Research Group, Szent Imre h. u. 112., Szombathely 9700, Hungary
[51] Institute of Astronomy, University of Cambridge, Madingley Road, Cambridge CB3 0HA, UK